Numerical Calculation of Doppler Steering Laws in Bi- and Multistatic SAR

J. Mittermayer, G. Krieger, *Fellow, IEEE*, and S. Wollstadt

Abstract — The paper defines Doppler steering laws for different bi- and multistatic acquisition geometries for Synthetic Aperture Radar (SAR). Central Swath Line (CSL) and Transmit Swath Line (TSL) acquisition geometries are introduced. Bistatic Zero Doppler Steering (BZDS) is defined. Multistatic acquisitions are classified into dedicated and supplementary types. Numerical approaches for the calculation of yaw, pitch and roll angles are described providing zero Doppler, constant Doppler and/or full Tx-Rx beam footprint overlap. The appendix provides an approximated analytical approach to calculate yaw and pitch angles to achieve a desired swath line.

I. INTRODUCTION

SAR mission design is increasingly taking advantage of the new possibilities that operate under the banner of *NewSpace*. NewSpace enables swarms of small, lightweight and cost-effective satellite platforms that allow the realization of large and variable SAR antenna structures distributed over several satellites. This offers the great advantage of flexible adaptation of the antenna configuration to different acquisition scenarios. For example, multiple baselines for interferometry and tomography can be generated simultaneously, e.g. [2], or swarms of SAR satellites can be configured in flight to either provide large area acquisitions or high geometrical resolutions, e.g. [3]. Current and future SAR mission concepts are therefore often spread over several satellites that execute multiple acquisition tasks simultaneously.

Another trend in SAR is the extension of existing SAR missions by small satellites to enhance the product variety with additional bi- and multistatic acquisitions. Several mission concepts have been proposed in the literature or are currently under development. Examples are SAOCOM-CS [14], PicoSAR [11] [12], SESAME [13], or SIGNAL [15].

The Doppler centroid is a fundamental parameter in SAR. In satellite SAR systems, it is mostly a consequence of the Earth's rotation. Smaller contributions are, for example, caused by antenna mis-pointing or attitude steering errors. These smaller contributions are hard to predict a priori, are specific for each mission and are typically minimized by system calibration. Therefore, they are not included here. The present paper focuses hence on the derivation of optimal Doppler steering values for nominal satellite formations where all satellite-specific pointing and attitude errors are neglected.

https://ieeexplore.ieee.org/document/9374566

A high Doppler centroid or a high variation thereof makes SAR processing, co-registration and geolocalization of SAR products difficult and complicated. Applications like SAR interferometry or tomography combine coherently multiple SAR images and suffer from a loss in azimuth spectral overlap due to different Doppler centroids in the individual images. In monostatic or quasi monostatic SAR systems, Total Zero Doppler Steering (TZDS) [1] is often used to reduce the Doppler centroid and its variation towards zero by applying a yaw and pitch steering that varies along the orbit. For example, TZDS is successfully employed in TerraSAR-X [8],[9] and TanDEM-X [10]. In [19], a stringent analytical derivation of TZDS based on satellite position and velocity vector is provided by introducing a relative velocity vector, which includes the velocity component of the Earth rotation. Another formulation for the TZDS yaw and pitch angles as a function of the osculating Kepler elements is provided in [19] and [20].

In [6], the ISO-Doppler steering is introduced. It assumes a monostatic TZDS for the Tx satellite, and a steering of the Rx satellite that aligns the receive antenna pattern along the bistatic iso-Doppler of the Tx-Rx SAR satellite pair by means of an additional pitch rotation. The paper at hand introduces Doppler steering approaches for different bi- and multistatic acquisition types. The approach for supplementary Doppler steering to Multiple Swath Lines introduced in section IV.B.2 is somehow similar to ISO-Doppler steering, but performs a combined yaw and pitch steering to achieve a constant bistatic Doppler centroid, followed by an additional roll steering that provides the beam overlap in range.

For previous space-borne bistatic SAR missions, such as the Shuttle Radar Topography Mission (SRTM) [18] and the TanDEM-X mission [10], the effect of antenna footprint (that means beam) alignment and the resulting impact on the Doppler centroid has been investigated, especially for the SAR interferometry performance. For TanDEM-X, [10] reports that, on the one hand, sufficient bistatic Tx and Rx beam footprint overlap goes along with a shift of 20% of the processed bandwidth between the monostatic and bistatic Doppler centroids. On the other hand, an independent TZDS for both satellites provides adequate monostatic and bistatic Doppler spectrum overlap but beam azimuth displacements of up to 1 km. However, in this case, the bistatic image suffers a gain reduction due to Tx and Rx beam mismatch. For TanDEM-X with its relatively small along-track baselines, it was decided to implement independent TZDS in both satellites. This paper deepens the discussion on the duality of footprint and Doppler overlap. It also extends this discussion to multistatic acquisitions.

The Doppler centroid is affected by the attitude angles yaw, pitch and roll, and their rotational sequence. In the paper, the sequence is first yaw, then pitch and finally roll, as is the case in [19] and [20]. Satellite system specific transformations and definitions need to be considered, too. For example, mechanical antenna offset angles or lever arms. In order to provide a general method, the paper provides numerical approaches that estimate the attitude angles required to point the antenna to those positions on ground, which have the desired bistatic Doppler centroid, preferably zero Hz. The numerical approaches are applied to one example system. Applying the numerical approaches to different systems, for example with different rotation sequence, will result in different steering angles, but the desired Doppler centroids will be obtained as well.

In the paper, no additional electronical or mechanical antenna steering was applied without loss of generality. All transmit and receive patterns were ground projected in their two-dimensional main lobes and the resulting projections were used to verify the pattern overlaps.

Section II defines the basic acquisition geometries Central Swath Line (CSL) and Transmit Swath Line (TSL) as well as a multistatic orbit example scenario that supports the discussion throughout this paper. Section II also illustrates the principal effect of the attitude angles yaw, pitch and roll on the antenna footprint, and gives an overview of the calculation of the bistatic Doppler centroid. Section III introduces an approach for Bistatic Zero Doppler Steering (BZDS) that is based on the CSL geometry. The approach calculates yaw, pitch and roll angles for the Tx and Rx satellites that provide both zero Doppler centroid and full overlap of Tx and Rx beam footprints. Section IV classifies multistatic acquisitions into dedicated and supplementary types, and modifies the BZDS approach towards multistatic acquisitions. Single and Multiple Swath Lines are introduced. Section V compares all bi- and multistatic steering laws as well as their performance in terms of bistatic Doppler centroid and ground beam overlap. In the appendix, an approximated analytical solution for multistatic yaw and pitch angles is given, together with an equation that describes the analytical dependence between Doppler centroid, squint, yaw, pitch and look angles, and the Earth rotational speed.

II. Bi- and Multistatic Geometries

A. Central and Transmit Swath Line Geometries

Figure 1 on the left depicts a Transmit Swath Line (TSL) geometry where the Tx satellite keeps its monostatic attitude steering. Assuming TZDS and a monostatic acquisition where the Tx satellite transmits and receives, the zero Doppler centroid arises for targets in the center of the Tx swath along the TSL. In the bistatic acquisition, the Rx satellite is ahead by a distance of D_{TR}. Each satellite follows its own steering law. The figure shows how the yaw, pitch and roll rotations are defined in the example SAR satellite system of the paper. The **z**-axes are oriented into negative satellite position vector direction, the **y** vectors into **z** x $\mathbf{V}_s$ direction, and the **x** vectors into **y** x **z** direction. The letter x denotes the cross product.

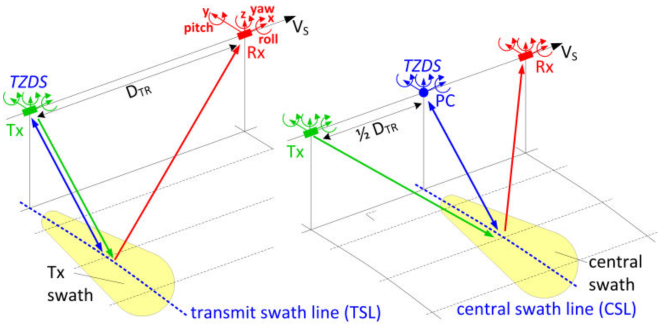

Figure 1 (left) Transmit swath line acquisition with Tx satellite applying monostatic TZDS and Rx satellite attitude steering towards the transmit swath line. (right) Central swath line acquisition geometry with Tx and Rx satellite steering towards the central swath line, which results from monostatic TZDS at the virtual phase center position PC. Each satellite applies its own steering law. The basic yaw, pitch and roll rotations are indicated.

Figure 1 on the right shows the bistatic Central Swath Line (CSL) acquisition geometry. The CSL is defined by a virtual monostatic acquisition from the bistatic phase center (PC) position that applies monostatic TZDS. The bistatic Doppler centroid is zero along the CSL, independent of the Tx and Rx incidence angles, considering the virtual monostatic acquisition from the PC [1].

B. Multistatic Orbit Formation Example Scenario

A multistatic example scenario is defined that encompasses several examples of bistatic transmit-receive geometries. A single Tx and four Rx satellites fly in formation. Rx_0 is the formation master satellite and flies a TerraSAR-X like orbit [7] at 514 km altitude. Rx_1, Rx_2 and Rx_3 (hereinafter referred to as Rx_i) fly close formation helix orbits around the Rx_0 orbit, similar to the TanDEM-X helix orbit [10]. Each of the receive satellites has a different across-track, radial and along-track baseline with respect to Rx_0. The helix orbits are characterized by the desired (nominal) maximum baselines in Earth-fixed geometry, which are illustrated in Figure 2. The Tx satellite follows Rx_0 on the Rx_0 orbit at an along-track distance of 15 km.

The orbits for the multistatic scenario were simulated as Kepler orbits, in principle as described in [10] for TanDEM-X. From the orbital baselines depicted in Figure 2, deltas in eccentricity and ascending node were derived for Rx_i, and the Kepler orbit parameters were modified accordingly. Figure 3 shows on the left side the nominal radial, cross-track, and along-track baselines from Rx_0 to Rx_i at the corresponding argument of latitude. On the right side of Figure 3, the along-track baselines between Tx and Rx_0, and Rx_i are shown. The Earth rotation introduces a non-compensable offset in the cross-track baseline, which causes small differences and the asymmetry in the simulated cross-track extreme values, shown in *Figure 3*, as compared to the nominal input values, shown in *Figure 2*.

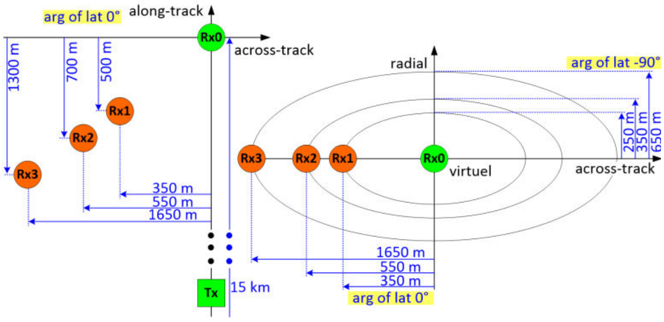

Figure 2 Characterization of the nominal orbit formation example scenario in Earth-fixed geometry. Five satellites fly in interlaced helix orbits. Rx_1, Rx_2 and Rx_3 in close formation around the Rx_0 orbit. Rx_0 and Tx fly on the same TerraSAR-X-like orbit. Tx follows Rx_0 in a greater along-track distance.

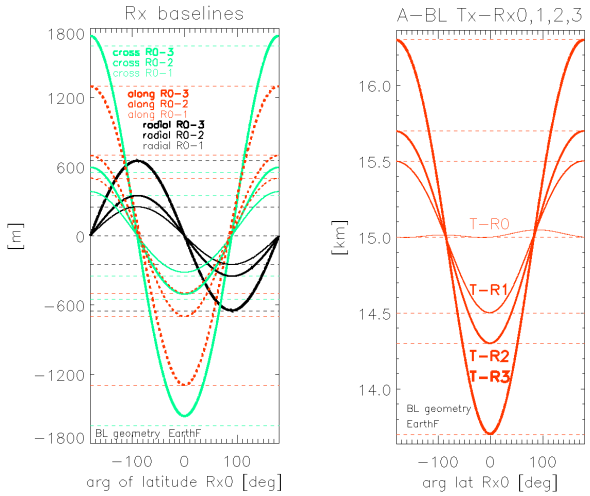

Figure 3 Baselines in Earth-fixed geometry of the simulated Kepler orbits as a function of the argument of latitude. (left) Baselines between receive satellites from Rx_0 to Rx_1, Rx_2 and Rx_3 in cross-track, along-track and radial directions. (right) Along-track baselines from Tx to Rx_0, Rx_1, Rx_2 and Rx_3. In both plots, the dashed horizontal lines identify the nominal extreme values of the baselines and the corresponding along-track separations.

C. Principal Effect of Yaw, Pitch and Roll Rotations

For a better understanding of the numeric approaches, Figure 4 shows the principal effect of yaw, pitch, and roll angle steering on the antenna footprints. The figure shows the ground projections of the Tx and Rx_0 satellite positions in black and light blue color, respectively. Both satellites fly the same TerraSAR-X orbit with Tx being behind Rx_0 by 15 km. The ground track of the satellites is indicated by the solid line. The dotted line is a parallel shift of the ground track. The ground footprints that result from single CSL steering in section IV.A.1 are on the right of the plot. All required transformations and the Earth rotation are considered. The antenna patterns for both satellites are generated as two-dimensional sinc-pattern with azimuth and elevation beam widths of 0.63° and 2°, respectively. The near range look angle is 15.27°. The Tx and Rx_0 pattern footprint lines are shown in black and light blue color, respectively, at a contour level of -6 dB. They overlap completely.

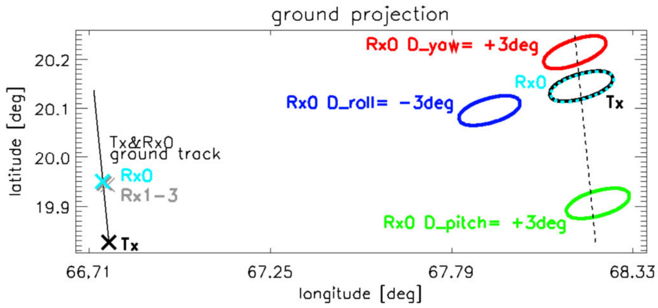

Figure 4 Effect of yaw-only, pitch-only, or roll-only angle offset on antenna footprints. Ground projections of Tx (black) and Rx_0 (light blue) satellite positions. Satellites ground track in solid line, parallel shifted ground track in dotted line. The flight or azimuth direction reflects the inclination of 97.4°.

Applying an offset of 3° to only the Rx_0 yaw angle results in the azimuth shifted red Rx_0 footprint. An offset of 3° applied to only the pitch angle results in the green Rx_0 footprint. Both yaw and pitch offsets cause mainly a shift in azimuth direction. In this example geometry, the pitch offset is more sensitive. An offset of -3° applied to only the roll angle of Rx_0 shifts the footprint towards near range. It is shown in blue color. It should be kept in mind that both yaw-only as well as pitch-only angle offsets result in footprint shifts mainly into azimuth direction.

Figure 4 also demonstrates the almost perfect overlap of the two-dimensional pattern main lobes in case of single swath line steering as the main lobes of the Tx and offset-free Rx_0 patterns completely overlap.

D. Calculation of the Bistatic Doppler Centroid

In monostatic SAR, the Doppler frequency f_D is defined by [1][5]

$$f_D = -\frac{2}{\lambda}\cdot\dot{r} = -\frac{2}{\lambda}\cdot\left(\sqrt{\vec{r}\cdot\vec{r}}\right)^{\cdot} = -\frac{2}{\lambda}\cdot\frac{\vec{r}\cdot\dot{\vec{r}}}{r}, \tag{1}$$

and the Doppler centroid f_{DC} is the center frequency of the Doppler or azimuth spectrum. In the monostatic illumination of *Figure 5*, shown in blue color, the target on-ground is observed by the radar. In (1), λ is the wavelength. The azimuth time dependent distance vector between platform and target is $\vec{r}$, $\dot{\vec{r}}$ means its derivative with respect to time, and r is its length. $\vec{r}$ is also often referred to as the slant range vector, and r as the slant range distance. At the center of the azimuth beam, the Doppler centroid f_{DC} can be defined as

$$f_{DC} = -\frac{2}{\lambda}\cdot\frac{\vec{r}\cdot\dot{\vec{r}}}{r} = -\frac{2}{\lambda}\cdot\left|\dot{\vec{r}}\right|\cdot\frac{\vec{r}\cdot\dot{\vec{r}}}{r\cdot\left|\dot{\vec{r}}\right|} = -\frac{2}{\lambda}\cdot v_S^{EF}\cdot\sin(\psi)\cdot \tag{2}$$

The squint angle ψ is defined to be π/2 minus the angle between $\dot{\vec{r}}$ and $\vec{r}$. In (2) and (3) below as well as in all the numerical Doppler centroid calculations carried out in this paper, $\vec{r}$ and $\dot{\vec{r}}$ are in the Earth fixed system (**EF**), and $\left|\dot{\vec{r}}\right|$ is the length of the Earth fixed satellite velocity vector $\vec{v}_S^{EF}$.

Monostatic TZDS means a satellite attitude steering that always orientates the boresight antenna direction perpendicular to the velocity vector in the Earth-fixed system [1]. This sets ψ to zero and aligns the satellite's along-track axis with its velocity vector.

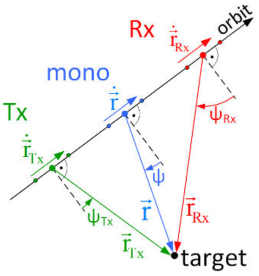

Figure 5 Point target observed by a monostatic radar (blue), and a bistatic radar's transmitter Tx (green) and receiver Rx (red). All satellites fly in the same orbit. The squint angle ψ indicates the direction that corresponds to the center of the illuminated azimuth spectrum, that is the Doppler centroid.

In the bistatic case with the transmitter (Tx) and the receiver (Rx) located on separate platforms, the Doppler frequency derives from the total radar signal path length variation with azimuth time. It is composed of different contributions from the transmit (r_{Tx}) and receive path length variations (r_{Rx}), whereas in the monostatic acquisition, the distance r is run through twice:

$$
\begin{aligned}
&2\cdot r \Rightarrow r_{Tx} + r_{Rx}\\
&2\cdot \dot{r} \Rightarrow \dot{r}_{Tx} + \dot{r}_{Rx}\\
&f_{DC,bi} = -\frac{1}{\lambda}\cdot\frac{\vec{r}_{Tx}\cdot\dot{\vec{r}}_{Tx}}{r_{Tx}} - \frac{1}{\lambda}\cdot\frac{\vec{r}_{Rx}\cdot\dot{\vec{r}}_{Rx}}{r_{Rx}} = f_{DC,Tx} + f_{DC,Rx}\,.\\
&\quad = -\frac{1}{\lambda}\cdot v_{S,Tx}^{EF}\cdot\sin\left(\psi_{Tx}\right) - \frac{1}{\lambda}\cdot v_{S,Rx}^{EF}\cdot\sin\left(\psi_{Rx}\right)
\end{aligned}
\tag{3}
$$

It is possible to define independent transmit and receive Doppler centroids $f_{DC,Tx}$ and $f_{DC,Rx}$, respectively. They add up to the bistatic Doppler centroid $f_{DC,bi}$. *Figure 5* shows the bistatic acquisition with the transmit and receive paths as well as the corresponding squint angles ψ_{Tx} and ψ_{Rx}.

The approaches provided in the following sections for the calculation of the Doppler centroid and the squint angle are based upon (3), and thus from $\vec{r}$, which is target position minus satellite position in the **EF** system. The target positions are calculated by intersecting the center azimuth beam illumination direction with the Earth surface. This direction depends on the attitude angles, the look angle θ_{lk}, and the Earth rotational speed ω_E. For the exemplary SAR system under consideration, the dependence of Doppler centroid and squint angle from yaw angle θ_{yaw} and pitch angle θ_{pitch} can be summarized as:

$$
\begin{aligned}
f_{DC}\left(\theta_{yaw},\theta_{pitch};\theta_{lk},\omega_E\right) &= -\frac{q}{\lambda}\cdot\vec{v}_S^{EF}\cdot\hat{\vec{r}}^{EF} = -\frac{q}{\lambda}\cdot v_S^{EF}\cdot\sin\left(\psi\right)\\
&= -\frac{q}{\lambda}\cdot v_{rel}^{I}\cdot\sin\left(\psi\right) = -\frac{q}{\lambda}\cdot\vec{v}_{rel}^{I}\cdot\hat{\vec{r}}^{I}\\
&= -\frac{q}{\lambda}\cdot\left(\dot{\vec{p}}^{I} - \vec{\omega}_E^{I}\times\vec{p}^{I}\right)\cdot {}^{I}T^{L}\cdot\begin{bmatrix}\cos\theta_{yaw}\cdot\sin\theta_{pitch}\cdot\cos\theta_{lk} - \sin\theta_{yaw}\cdot\sin\theta_{lk}\\ \sin\theta_{yaw}\cdot\sin\theta_{pitch}\cdot\cos\theta_{lk} + \cos\theta_{yaw}\cdot\sin\theta_{lk}\\ \cos\theta_{pitch}\cdot\cos\theta_{lk}\end{bmatrix}
\end{aligned}
\tag{4}
$$

with $q = 2$ for monostatic

$q = 1$ for both bistatic Doppler components $f_{DC,Tx}$ and $f_{DC,Rx}$

where ${}^{L}T_{SL}^{I}$ denotes the transformation matrix from the local system (**L**) into the inertial system (**I**), and $\vec{p}^{I}$ is the inertial position vector of the satellite with origin at the Earth center. The symbol ^ means unit vector. The first line of (4) defines the squint angle ψ in the Earth-fixed system with the scalar product of satellite velocity vector and slant range vector. The second line defines ψ in the inertial system. The relative velocity vector $\vec{v}_{rel}^{I}$ is defined in [19]. It is explained in appendix.A, where also the equivalence of the velocities v_{rel}^{I} and v_S^{EF} is shown. The last line of (4) is derived in appendix.C.

III. Bistatic Total Zero Doppler Steering (BZDS)

Provided that the Tx and Rx satellites can freely adjust their attitude, the task of BZDS is to minimize the bistatic Doppler centroid $f_{DC,bi}$ and its variation along the image range dimension as close to zero Hz as possible. This section provides an approach to derive the BZDS yaw, pitch and roll angles for the Tx and Rx satellites. It is based on the CSL of section II.A, which provides zero Doppler centroid for the acquisition from the monostatic PC position. This CSL also provides zero Doppler centroid for a bistatic acquisition with the same PC_0 position, which is the phase center produced by the separated Tx and Rx_0 positions as is shown in Figure 6.

The key idea is to use the two degrees of freedom in the attitude steering – yaw and pitch cause mainly an azimuth shift of the footprint – to point the antenna beam in near and far range onto the CSL, which indicates the target locations of zero Doppler. Then the roll angle is used to adjust the desired acquisition look angles. The approach is a two-step process:

1) For a look angle range of interest calculate the on-ground target positions with minimum $f_{DC,bi}$ that define the CSL.
2) Numerically estimate the Tx and Rx_0 attitude steering laws that align the Tx and Rx_0 antenna footprints along the CSL.

The BZDS block diagram is shown in Figure 7. The virtual PC_0 position is calculated from the current Tx and Rx_0 orbit positions. Then, several ground intersection points (IC) are calculated from the PC_0 position using monostatic TZDS. This defines the CSL that is shown in the acquisition geometry of Figure 6 in green color. The line follows the Earth curvature.

The next step is the numerical estimation of the receive satellite yaw and pitch angles $\theta^*_{yaw,Rx}$ and $\theta^*_{pitch,Rx}$ that minimize both the distances $dist_{az,near}$ and $dist_{az,far}$ between the CSL and the intersection points IC_{near} and IC_{far} (refer to Figure 6). In this paper, an asterisk * indicates the result of a numerical estimation. The subscripts near and far correspond to the look angles $\theta_{lk,near}$ and $\theta_{lk,far}$, respectively. During the estimation, for many combinations of yaw and pitch angles the antenna pointing is calculated following the SAR system specific definitions (sequence of rotations, lever arms, etc.) and from the antenna pointing the current IC_{near} and IC_{far} are calculated.

The transmit yaw and pitch angles $\theta^*_{yaw,Tx}$ and $\theta^*_{pitch,Tx}$ are estimated in the same way. The angle estimations in Tx and Rx are independent of each other. They depend on the respective Tx and Rx satellite positions and the common CSL.

At $\theta_{lk,near}$ and $\theta_{lk,far}$, the bistatic Doppler centroid becomes zero. The Earth curvature causes the Doppler centroid to slightly deviate from zero at other look angles. The example in the next sections shows that an appropriate selection of $\theta_{lk,near}$ and $\theta_{lk,far}$ is in-between the center look angle $\theta_{lk,cent}$ and the limits of the desired look angle access range.

Figure 8 shows, as an intermediate result of the Tx attitude angle estimation, the azimuth distances $dist_{az,near}$ and $dist_{az,far}$ as a function of yaw and pitch angles. The contour plot on top provides a slice at an azimuth distance of 0 m. It shows two lines, one for $dist_{az,near}$ and one for $dist_{az,far}$. The intersection of these two lines provides the desired angles $\theta^*_{yaw,Tx}$ and $\theta^*_{pitch,Tx}$.

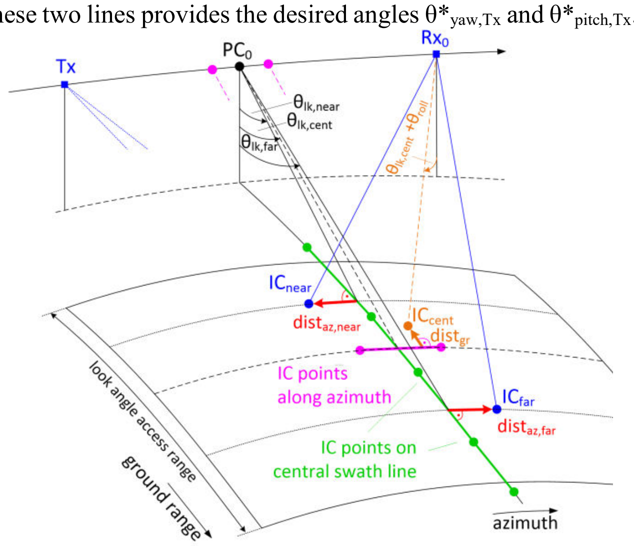

Figure 6 Estimation of BZDS yaw, pitch and roll angles for Rx_0 satellite. Yaw and pitch angles are estimated by minimization of the distances $dist_{az,near}$ and $dist_{az,far}$. The roll angle is estimated by minimization of the distance $dist_{gr}$.

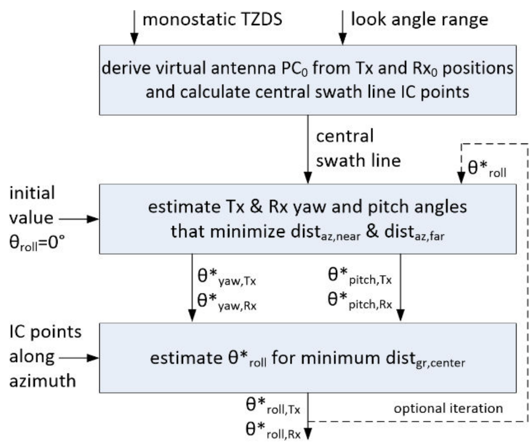

Figure 7 Approach for Bistatic Zero Doppler Steering (BZDS) estimation.

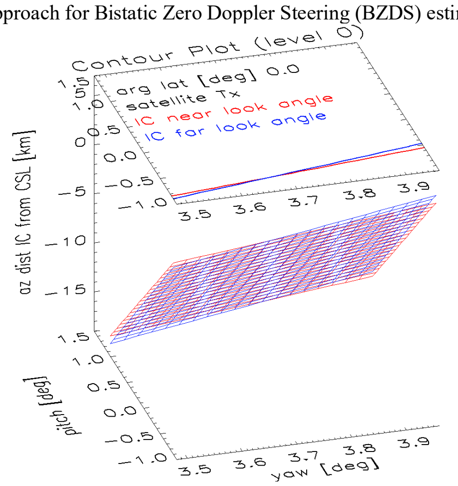

Figure 8 Distances $dist_{az,near}$ (red) and $dist_{az,far}$ (blue) as a function of yaw and pitch angle at 0° argument of latitude for the transmit satellite.

In the last stage of Figure 7, the roll angle is estimated. As Figure 6 shows in pink color, from orbit positions left and right of PC_0, on-ground IC points are calculated for the center look angle $\theta_{lk,cent}$ applying TZDS. These IC points define a line along the azimuth direction. The roll angle θ^*_{roll} is computed by minimization of the ground range distance $dist_{gr}$ of the center look angle intersection point IC_{cent} to that line along azimuth. The estimation is carried out independently for the Rx and Tx satellite positions applying the yaw and pitch angles that were estimated in the previous stage.

The calculation of the attitude steering angles as described so far provides already excellent results in terms of Doppler centroid and transmit-receive footprint overlap. This can be seen from the results for the example scenario that are shown in Figure 15 in the result section V. Since both yaw and pitch angles mainly cause ground beam azimuth shifts, two degrees of freedom are available for the yaw and pitch estimation. In Figure 7, the Tx and Rx roll angles are thus initially set to zero in the calculation of the Tx and Rx yaw and pitch angles. With extreme geometries, however, a further iteration can be carried out. This is indicated in Figure 7 by feeding the estimated roll angles θ^*_{roll} for the Tx and Rx satellites back into the yaw and pitch angle computation stage.

For the example multistatic scenario of section II.B, Figure 14 shows the BZDS angles that result for bistatic acquisition by the Tx and Rx_0 satellites.

IV. Multistatic Acquisition Types

Figure 9 provides an overview of the different multistatic acquisition types and attitude steering approaches that are discussed in this section. Multistatic acquisitions can be divided into *dedicated* and *supplementary* ones. Dedicated connotes that the Tx and Rx satellites as well as the attitude steering laws are designed for multistatic operation.

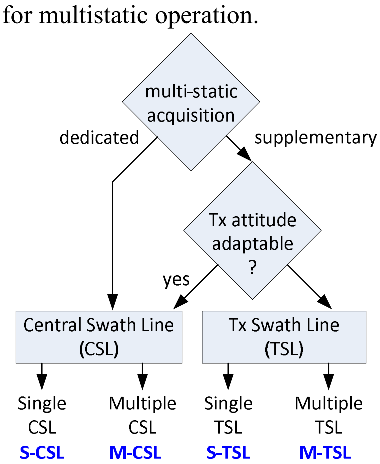

Figure 9 Dedicated and supplementary multistatic acquisition types.

Dedicated acquisitions should preferably be designed in CSL geometry since it is able to provide a zero bistatic Doppler centroid. An example mission concept is MirrorSAR [2] that is designed from the beginning as a mission with multistatic acquisitions. Dedicated multistatic acquisitions are discussed in section A in the variants Single CSL (S-CSL) and Multiple CSL (M-CSL). In the first variant, the Tx and Rx_i footprints fully overlap and the Doppler centroids can be optimized to be symmetric to zero Hz. In M-CSL, the Doppler centroids are minimized to zero Hz but the Tx and Rx_i footprints do not completely overlap.

Supplementary acquisitions are based on a classical monostatic SAR mission that provides the transmitter. It is supplemented by additional receiving satellites, which were not accounted for during the initial monostatic mission design. If the Tx mission is able to adapt its attitude steering to multistatic acquisitions, the CSL geometry should also be used. If not, the Tx mission keeps to its monostatic attitude steering and the TSL geometry applies, which implies high bistatic Doppler centroids. An example is the PicoSAR mission concept [11]. Supplementary acquisitions in TSL geometry are discussed in section B in the approaches Single TSL (S-TSL) and Multiple TSL (M-TSL).

A. Dedicated Multistatic Steering

In a multistatic scenario with a single Tx and several Rx satellites it is not possible to achieve for all bistatic Tx-Rx_i combinations both zero Doppler and full Tx and Rx footprint overlap as well. Full overlap for all combinations is only possible by different BZDS laws corresponding to different CSLs. However, the Tx satellite can only be steered into one specific attitude at a specific point in time, and thus only to a unique CSL. Below in subsection 1, the BZDS is expanded to a multistatic scenario by keeping full footprint overlap, and introduces in subsection 2 a method to minimize the absolute f_{DC} values. Subsection 3 investigates the consequences of allowing multiple CSLs.

1) Single Central Swath Line (S-CSL)

BZDS is applied to all bistatic combinations Tx-Rx_i of the multistatic example scenario, with $i \in \{0,1,2,3\}$. The application of the same virtual antenna phase center PC_0 from the Tx-Rx_0 acquisition to all bistatic acquisitions results in the attitude steering angles of *Figure 14* plotted in continuous line style. The corresponding beam deviations and bistatic Doppler centroids are provided in *Figure 15*.

The variation of the different bistatic Doppler centroids are inherent to the multistatic scenario in case of complete Tx and Rx_i footprint overlap. They are enforced by the different Rx_i satellite positions, which on the other hand, provide the desired Rx orbital baselines. The multistatic example geometry based on helix orbits causes additionally a variation of the Doppler centroid differences along the orbit. Since the Doppler centroid differences are dominated by the along-track separation of the Rx-satellites, they have a maximum at the equator where the Rx-satellites of the example orbit formation scenario are furthest apart in along-track. Referring to *Figure 3*, the 19.9° argument of latitude in *Figure 15* is close to the maximum of the Doppler centroid differences at the equator.

2) S-CSL from Midpoint Phase Center PC_m

Doppler centroid differences cannot be avoided in multistatic S-CSL steering. However, the maximum absolute Doppler centroid values can be optimized by selection of a proper common CSL. Figure 10 shows the satellite formation of the example scenario and the phase centers PC_i of the bistatic acquisitions at an arbitrary position along the orbit. This paper proposes to use a Midpoint Phase Center PC_m to define the S-CSL. For the estimation of PC_m, the minimum and maximum distances between Tx and the PC_i positions are determined. PC_m is then set to the position in-between the two PCs that belong to this minimum and maximum distances. The S-CSL for the desired look angle range can then be derived from the PC_m position and monostatic TZDS. Figure 14 shows the resulting S-CSL attitude steering angles as dashed lines. In Figure 15, it can be seen that the footprints fully overlap. The extreme values of the Doppler centroids are reduced and are symmetrical to zero Hz. Additionally, the maximum Doppler centroid variation versus range is reduced, which is considered as an advantage in SAR processing.

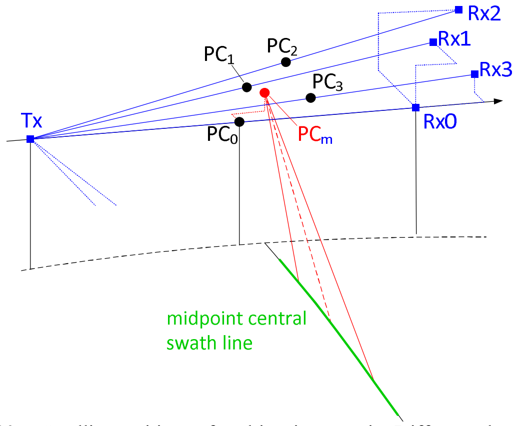

Figure 10 Satellite positions of multistatic scenario. Different phase centers PC_i result from each Tx-Rx_i combination. The S-CSL is derived from the midpoint phase center PC_m.

3) Multiple CSLs (M-CSL)

If multiple CSLs are allowed, this will result in a loss of footprint overlap. Figure 11 illustrates a M-CSL geometry with an increased Tx beam width to account for the loss in footprint overlap. Eq. (3) implies that for each slant range position there must be a combination of squint angles ψ_{Txi} and ψ_{Rxi} that produces equal squint angle sums. For example, in *Figure 11*, $\psi_{Tx1} + \psi_{Rx1}$ equals to $\psi_{Tx2} + \psi_{Rx2}$, and thus the bistatic Doppler centroids $f_{DC,bi1}$ and $f_{DC,bi2}$ are equal to each other, too. The non-overlapping CSLs for Tx-Rx_1 and Tx-Rx_2 and the corresponding Doppler centroids are depicted in the figure.

Due to the displaced footprints, the bistatic signals Tx-Rx_1 and Tx-Rx_2 are not acquired simultaneously but shifted in azimuth time. This shift is typically a few hundredths to tenths of a second. The target marked by a circle in the figure is acquired first in the combination Tx-Rx_2, and shortly after by the combination Tx-Rx_1. In figurative terms, different parts of the wider Tx beam are cut out by the different Rx beams. This allows for equal bistatic Doppler centroids in the individual bistatic acquisitions through different $f_{DC,Txi}$. Since the ground footprints do not fully overlap, there are losses and differences in the signal gains of the individual acquisitions. It is not possible to cut out a small Tx beam from wider and displaced Rx beams. The cut areas would be identical and would result in a single CSL. Thus, multiple CSLs require multiple Tx illuminations at once - or a wider Tx beam.

Figure 12 provides the block diagram of the M-CSL steering angle calculation. Since multiple swath lines are allowed, the numerical estimation of the attitude angles cannot be driven by the adjustment of all beams to one swath line. Thus, the estimation directly minimizes the Doppler centroid.

In the first stage, the midpoint phase center PC_m is estimated with its monostatic TZDS attitude angles as described in the previous section. In the second stage, for the PC_m position, the corresponding ground intersection point at center look angle $IC_{cent,m}$ is derived. From $IC_{cent,m}$ and the Tx satellite position the Tx Doppler centroid $f_{DC,Tx}$ is calculated to be the reference for the estimation in stage three.

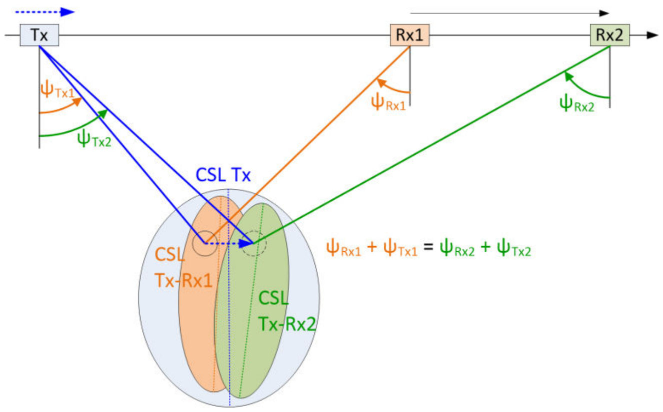

Figure 11 Multiple Central Swath Lines (M-CSL) in central swath geometry. The smaller Rx footprints cut out parts of the wider Tx footprint. This allows for equal bistatic Doppler centroids. The acquisitions of a target occur with a small azimuth time shift. There are gain losses due to not fully overlapping beams.

Stage three estimates the Tx satellite yaw and pitch angles by minimizing the differences between the Tx near and far Doppler centroids $f_{DC,Tx,near}$ and $f_{DC,Tx,far}$, respectively, to the reference $f_{DC,Tx}$ (cf. third block in Figure 12). The output angles $\theta^*_{yaw,Tx}$ and $\theta^*_{pitch,Tx}$ define the CSL in Tx.

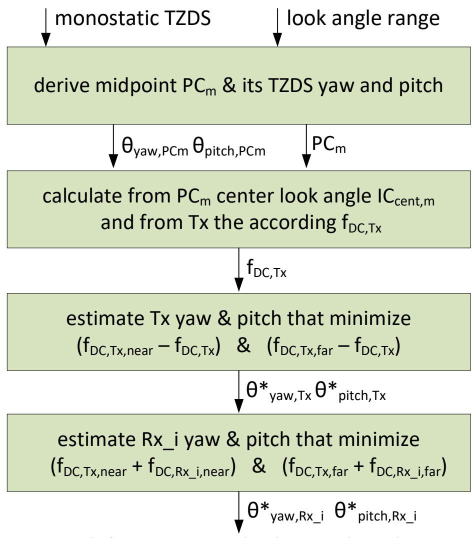

Figure 12 Approach for M-CSL steering in central swath geometry.

In the last stage, the individual yaw and pitch angles of the Rx_i satellites are estimated by minimization of both the bistatic near and far Doppler centroids. The attitude steering angles for the example scenario as obtained from M-CSL steering are shown in *Figure 16*. *Figure 17* provides the resulting "zero" Doppler centroid and the deviations in footprint overlaps.

B. Supplementary Multistatic Steering

This section discusses supplementary acquisitions, in which the Tx satellite is unable or not allowed to modify its monostatic attitude steering. Hence, the TSL geometry applies. The Rx satellites exploit the Tx radar signal, but there is no collaboration with the Tx satellite in terms of attitude steering.

1) Single Transmit Swath Line (S-TSL)

The BZDS approach of section III can be utilized to align the Rx footprints to the TSL (refer to *Figure 1*), and thus to overlap them with the Tx footprint. *Figure 18* provides the corresponding steering law for the example scenario, and *Figure 19* contains the beam azimuth displacements and the bistatic Doppler centroids.

2) Multiple Transmit Swath Line (M-TSL)

The approach of *Figure 12* for dedicated acquisitions works for supplementary acquisitions in M-TSL steering, too. A few modifications are necessary. *Figure 13* shows the block diagram of the modified approach. The Tx yaw and pitch angles are fixed, and the center look angle intersection point $IC_{cent,Tx}$ is determined from the Tx position and TZDS. The Tx and Rx_i centroids $f_{DC,Tx}$ and $f_{DC,Rxi}$ are calculated with respect to this intersection point. The mean Doppler centroid f_{DC,Bi_mean} is then calculated similar to the calculation of PC_m in section IV.A.2. It is the mean value of the minimum and maximum Doppler centroids f_{DC,Bi_i}.

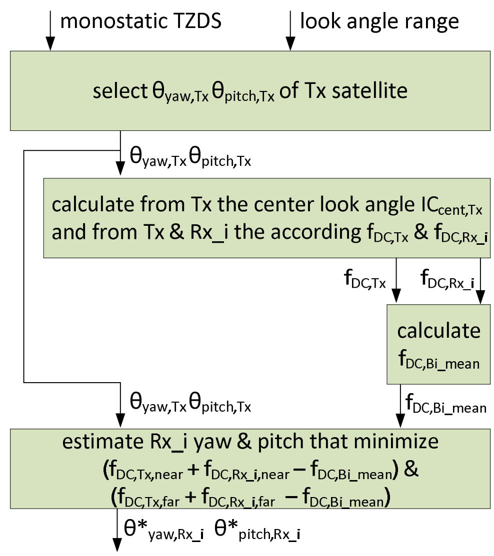

Figure 13 Modified block diagram for M-TSL steering in supplementary acquisitions (cf. Figure 12).

The Tx yaw and pitch angles are ingested into the last stage of the block diagram in *Figure 13*, in which the Rx_i yaw and pitch angles are obtained by minimizing the differences between the bistatic near and far Doppler centroids to f_{DC,Bi_mean}.

Figure 20 and *Figure 21* provide the steering angles, the resulting Doppler centroids and the azimuth beam overlap for M-TSL in supplementary acquisition.

V. Resulting Steering Laws, Doppler Centroids and Beam Overlaps

This section provides the resulting Doppler steering laws for the different bi- and multistatic approaches discussed in the previous sections. The steering laws were calculated for the example geometry introduced in section II.B. The performance of the different approaches is discussed in terms of bistatic Doppler centroid and ground beam overlap. The results for the Bistatic Zero Doppler Steering (BZDS) are a subset of the multistatic results in section IV.A.1.

A. BZDS and Dedicated Multistatic Steering

1) Bi- and Multistatic Single Central Swath Line (S-CSL)

Figure 14 shows the *BZDS attitude steering angles* in continuous line style in blue and green color. The bistatic Tx-Rx_0 acquisition geometry was applied, and the BZDS yaw, pitch and roll angles were calculated along the orbit. At each orbital position, the Tx and Rx_0 satellites are steered so that their ground footprints align with the CSL derived for that orbital position. The figure also shows the TZDS attitude angles for a virtual monostatic acquisition from PC_0, which is the phase center belonging to the Tx and Rx_0 satellites. The bistatic yaw angles are close to the monostatic ones. The pitch angles differ by about 0.8°, with opposite signs for the Tx and Rx_0 satellites. This causes the Rx_0 beam to be shifted backward and the Tx beam to be shifted forward to the CSL geometry of Figure 1 on the right side. The bistatic roll angle is small compared to yaw and pitch angles but it is required for full overlap of the Tx and Rx_0 beams.

The BZDS law is verified by the ground footprint displacement and the bistatic Doppler centroid $f_{DC,bi}$ in the simulated multistatic orbit formation example. Figure 15 shows the displacements at an orbit position of 19.9° argument of latitude. This argument of latitude has been selected as it is close to the equator where the values of the steering angles are high compared to the poles. Plot (a) presents in on-ground longitude and latitude coordinates the 3dB contour lines of the footprints of the monostatic illumination from PC_0 position with TZDS, and the Tx and Rx_0 footprints from the bistatic acquisition applying BZDS. The azimuth beam is simulated as a sinc-pattern with a 3dB beam width of 0.63°, sufficient for 1.5 m resolution in the X-band example geometry. The elevation beam is simulated by a rect-pattern for better visualization with a width of 20° in elevation or look angle. All the three footprints are congruent as well as the 3dB azimuth/elevation sample target positions that are marked by triangles or crosses.

Plot (b) of Figure 15 shows the azimuth displacement of the Tx and Rx_0 footprints in black and blue color, respectively. The displacements are with respect to the CSL. As expected, the minima occur at 31.5° and 41.5° look angles, which are the angles $\theta_{lk,near}$ and $\theta_{lk,far}$ that were used in the BZDS steering angle estimation. Plot (c) provides the Tx and Rx_0 Doppler centroids $f_{DC,Tx}$ and $f_{DC,Rx0}$, which were calculated as described in (3) from the target positions on the CSL and the Tx and Rx_0 satellite positions. It also shows $f_{DC,bi}$, being the sum of $f_{DC,Tx}$ and $f_{DC,Rx0}$. It is almost zero Hz.

The steering laws for multistatic *S-CSL steering based on the phase center PC_0* are provided in *Figure 14* in continuous line style. These steering angles cause the beam deviations and bistatic Doppler centroids of *Figure 15*. Plot (a) shows that all beam footprints coincide. This can also be seen by the pretty small azimuth displacements from the S-CSL in plot (b). As shown in plot (d), the Doppler centroids from the various bistatic combinations differ by up to 500 Hz. This is, for the example of the X-band SAR system, equivalent to 12 % of the azimuth processed bandwidth of 4150 Hz that is required for achieving an azimuth resolution of 1.5 m.

2) S-CSL From Midpoint Phase Center PC_m

The attitude steering angles that are based on the midpoint phase center PC_m are plotted in dashed line style in Figure 14. *Figure 15* shows in the plots (b) and (d) the corresponding azimuth beam displacements and the bistatic Doppler centroids, respectively. Since all satellites point to the same S-CSL, all beam footprints overlap fully. In plot (a), the dashed lines for PC_m are overlaid by the ones for PC_0 and thus not visible. The extreme values of the Doppler centroids for all the Tx-Rx_i combinations in plot (d) shown for PC_m in dashed line style are lower than the ones for PC_0 in continuous line style, and symmetrical to zero Hz. Additionally, the Doppler centroid variation of Tx-Rx_3 is reduced from 130 Hz for PC_0-based steering to 60 Hz for PC_m-based steering.

3) Multiple CSL (M-CSL)

Figure 16 provides the resulting attitude angles for Multiple Central Swath Line Steering. The bistatic Rx_i yaw angles are similar to each other and close to the monostatic yaw angle. The bistatic Tx yaw angle is about half a degree higher than the monostatic yaw angle at the ascending and descending equator. The Tx pitch angle is around -0.5°. The Rx pitch angle is around 0.8° and similar to the S-CSL pitch angles of Figure 14 for full footprint overlap. Figure 17 (a) shows the footprint misalignment for M-CSL steering, for a 20° look angle range from 26.5° to 46.5° and a 3 dB azimuth beam width of 0.63° that extends 7.2 km along the azimuth direction on ground. The deviation in the footprint overlaps increases towards near and far range. Figure 17 (b) shows the deviation of the individual Rx beams from the Tx beam. If the Tx beam should cover within its 3 dB beam width the maximum of 2.5 km Rx beam variations, it needs to be widened by 35%. Considering an imaging geometry with a smaller look angle range, the required widening of the Tx beam is less. For the example of 20 km ground beam width at 40° center incidence angle, the corresponding ground footprints are shown in Figure 17 (c). Furthermore, Figure 17 (b) indicates within the vertical lines a look angle range of 1.34° that corresponds to the 20 km swath. From these vertical lines, an Rx beam deviation of 750 m can be estimated. This corresponds to a required Tx beam widening of 10%. For comparison, *Figure 17* (c) includes additionally the footprint obtained for S-CSL steering using the PC_m in purple color. The positioning is similar since it is also based on the PC_m position. *Figure 17* (d) shows the resulting bistatic f_{DC} values for 20° look angle range in the different bistatic Tx-Rx_i combinations. All Doppler centroids are close to zero Hz - at the price of reduced footprint overlaps.

B. *Supplementary Multistatic Steering*

1) Single Transmit Swath Line (S-TSL)

For supplementary multistatic steering to a S-TSL, Figure 18 provides the steering angles resulting for the example scenario. Of course, the Tx steering angles are identical to the monostatic TZDS attitude angles. The yaw angles of the Rx_i satellites are similar to each other and are slightly higher than the Tx ones. The Rx_i pitch angles are about twice as large as those of the S-CSL in Figure 14. Figure 19 provides the corresponding beam azimuth displacements and the bistatic Doppler centroids. The Tx / Rx_i beam alignment shows only 50 m azimuth deviation in the plot of Figure 19 (b). The bistatic Doppler centroid in plot (c) is in the order of -5 kHz. This is expected since, due to TZDS, $f_{DC,Tx}$ is zero, and the $f_{DC,Rxi}$ are required to be about twice the value of Figure 15 (c). The Rx_i satellites need to steer twice as much backward into azimuth direction (cf. Figure 1). The Doppler centroids show a variation of about 1500 Hz within the 20° of look angle range. At a fixed look angle, the bistatic acquisitions differ in Doppler centroid by about 450 Hz.

2) Multiple Transmit Swath Line (M-TSL)

Figure 20 provides the resulting steering angles for M-TSL in supplementary acquisition. Monostatic and Tx steering angles are identical. The Rx_i yaw angles are similar to each other and smaller than the Tx ones. The Rx pitch angles are about 1.25°, and smaller than in the S-TSL steering that are shown in Figure 18. Figure 21 shows the beam alignments and bistatic Doppler centroids. The beam displacements are almost identical to the S-TSL steering of Figure 17. They correspond to about 35% loss in processed azimuth bandwidth for a 20° look angle range, and to 10% for a 20 km swath. The bistatic f_{DC} in Figure 21 (c) is about -5 kHz but there is almost no alteration in different bistatic Doppler centroids. The variation of all centroids versus look angle is reduced to 50 Hz.

C. *Multistatic Doppler Centroid Along the Orbit*

Figure 3 provides the Rx baselines variations and the distance variations between Tx and the Rx satellites as a function of argument of latitude. All attitude angles for the discussed steering laws are additionally provided versus the argument of latitude. This allows a view of the change in yaw, pitch and roll angles for different orbit positions with different baselines. This section supplements the footprint displacement and bistatic Doppler centroid results at several different orbit positions. For the case of M-CSL steering, *Figure 22* includes the results at the orbit positions of 0°, 40°, 85°, and -40° argument of latitude. The bistatic Doppler centroid and its variation with range are always close to zero Hz. The maximum azimuth displacement occurs close to the equator. However, the azimuth displacement with respect to the Tx-beam does not show a large variation along the orbit. The displacement between the Rx footprints is small at the poles where the Rx along-track baselines are minimum in the multistatic example scenario of section II.B.

VI. Conclusion

The Center Swath Line (CSL) and Transmit Swath Line (TSL) geometries for bi- and multistatic SAR imaging were defined. Starting from the monostatic definition, the bistatic Doppler centroid was formulated. It is composed of transmit and receive Doppler centroids. An approach was presented which numerically estimates yaw, pitch and roll angles for Bistatic Zero Doppler Steering (BZDS). The paper suggests a classification of multistatic acquisitions into dedicated and supplementary ones and provides steering approaches for both types.

In case of dedicated bistatic acquisitions, a zero Doppler centroid is obtained as well as full Tx and Rx footprint overlap by using the BZDS. A bistatic Doppler steering in TSL geometry is a special case of multistatic acquisitions with only a single Rx satellite. It is therefore covered by the presented multistatic steering approaches. Considering multistatic acquisitions with more than two Rx satellites it is impossible to achieve a zero Doppler centroid and full footprint overlap for all Tx and Rx footprints. Allowing deviations in the footprint overlaps, a zero Doppler centroid can be achieved in case of the CSL geometry. In TSL geometry, a constant Doppler centroid can be obtained. The deviations in the footprint overlap seem to be acceptable for the presented multistatic example scenario in X-band with 1.5 m azimuth resolution. However, the deviations need to be carefully studied for other scenarios and parameters. It depends on the application whether a full footprint overlap, a common Doppler centroid, or a trade-off between the two provides the best results. The presented TSL methodology for calculating the multistatic Rx yaw and pitch angles from those of the Tx geometry can be generalized. Even if the Tx satellite is not illuminating in TSL geometry, a constant multistatic Doppler centroid can be achieved along range. A possible application for this is forward or backward looking multistatic SAR.

For several transmit-receive combinations the attitude angles yaw, pitch and roll were calculated along the orbit. The verification of the steering approaches was performed by the projection of the transmit and receive beams onto the ground, and by numerically calculating the bistatic Doppler centroid. It has been demonstrated that the principle of optimizing the yaw and pitch angles using two slant ranges is generally valid. It can be applied to all kinds of acquisition geometries. One example is a forward reflection scenario.

One way to implement the proposed steering laws into a SAR mission is to calculate the laws on-ground for a certain satellite configuration, for example the five satellites of the example orbit configuration, along the orbit. Then Look-Up-Tables (LUT) for the yaw, pitch and roll angles can be stored on-board as a function of argument of latitude. In case of a new orbit configuration or acquisition geometry, for example switching from TSL to CSL or changing the maximum baselines between transmit and receive satellites, a new set of LUTs can be uploaded.

The appendix provides an approximated analytical solution to calculate multistatic yaw and pitch angles that achieve a desired swath line. It also relates the Doppler centroid and the squint angle analytically to the yaw, pitch and look angles and the Earth rotational speed. Appendix.B can be used to approximately calculate the multistatic attitude angles for Single Swath Line steering. This might be useful for a real-time on-board Doppler steering calculation. However, the real-time satellite position and velocity information of the Tx and the respective Rx_i satellite needs to be available on-board the satellites. Additionally, the on-board inclusion of a Digital Elevation Model (DEM) is considered to be difficult. The numerical calculation of the multistatic Doppler steering law on-ground is more accurate and a DEM can easily be introduced.

APPENDIX

The appendix provides an approximated analytical solution for the multistatic yaw and pitch angles in Single Swath Line Steering. Additionally, an equation is provided that describes the dependencies between Doppler centroid, squint, yaw, pitch and look angles, and the Earth rotational speed.

A. Nomenclature and Monostatic TZDS

In [19], a stringent analytical derivation of the monostatic TZDS is provided. We take this as a starting point for the multistatic derivation and use similar symbols and notations. A relative velocity vector $\vec{v}_{rel}^{I}$ in the Inertial System (**I**) that includes the velocity component of the Earth rotation is derived in [19]:

$$\vec{v}_{rel}^{I} = \left(\dot{\vec{p}}_{SL}^{I} - \vec{\varpi}_{E}^{I} \times \vec{p}_{SL}^{I}\right) \text{ with } \vec{\varpi}_{E}^{I} = \begin{bmatrix}0 & 0 & \omega_E\end{bmatrix}^T, \tag{5}$$

with $\vec{p}$ being the position vector of the satellite originating in the Earth center, the superscript I indicating the inertial system, and ω_E being the Earth rotational speed. The subscript SL indicates the orbit position SL_{OP} at which the Swath Line (SL) is calculated by applying monostatic TZDS. It can be shown that $\vec{v}_{rel}^{I}$ is the satellite velocity in the Earth fixed (**EF**) system $\vec{v}_{S}^{EF}$ transformed into **I**:

$$^{EF}T^{I}(\omega_E t) = \begin{bmatrix} \cos(\omega_E t) & \sin(\omega_E t) & 0 \\ -\sin(\omega_E t) & \cos(\omega_E t) & 0 \\ 0 & 0 & 1 \end{bmatrix},$$

$$\begin{aligned}
\left\langle \dot{\vec{p}}^{EF} \right\rangle^{I} &= {}^{I}T^{EF}(\omega_E t)\cdot \dot{\vec{p}}^{EF} = \left[{}^{EF}T^{I}(\omega_E t)\right]^{-1}\cdot\left[{}^{EF}\dot{T}^{I}(\omega_E t)\cdot\vec{p}^{I} + {}^{EF}T^{I}(\omega_E t)\cdot\dot{\vec{p}}^{I}\right] \\
&= \begin{pmatrix} \cos(\omega_E t) & -\sin(\omega_E t) & 0 \\ \sin(\omega_E t) & \cos(\omega_E t) & 0 \\ 0 & 0 & 1 \end{pmatrix} \cdot \begin{pmatrix} -\omega_E\cdot\sin(\omega_E t) & \omega_E\cdot\cos(\omega_E t) & 0 \\ -\omega_E\cdot\cos(\omega_E t) & -\omega_E\cdot\sin(\omega_E t) & 0 \\ 0 & 0 & 0 \end{pmatrix}\cdot\vec{p}^{I} + \dot{\vec{p}}^{I} \\
\left\langle \dot{\vec{p}}^{EF} \right\rangle^{I} &= \left\langle \vec{v}_{S}^{EF} \right\rangle^{I} = -\omega_E \cdot \begin{pmatrix} 0 & -1 & 0 \\ 1 & 0 & 0 \\ 0 & 0 & 0 \end{pmatrix}\cdot\vec{p}^{I} + \dot{\vec{p}}^{I} = \begin{bmatrix} 0 \\ 0 \\ -\omega_E \end{bmatrix} \times \vec{p}^{I} + \dot{\vec{p}}^{I} = -\vec{\varpi}_{E}^{I}\times\vec{p}^{I} + \dot{\vec{p}}^{I} = \vec{v}_{rel}^{I}
\end{aligned} \tag{6}$$

where $^{EF}T^{I}(\omega_E \cdot t)$ is the time (t) dependent rotation matrix from **I** into **EF**, and $\langle\ \rangle^{I}$ transforms into **I**. Since $^{EF}T^{I}$ is a rotation matrix, the vector lengths v_{S}^{EF} and v_{rel}^{I} are equal.

In our paper, a column vector $\vec{a}_{SL}^{B}$ in the Body System (**B**) is obtained from $\vec{a}_{SL}^{L}$ in the Local System (**L**) by the rotation sequence first yaw angle $\theta_{yaw,SL}$, then pitch angle $\theta_{pitch,SL}$, and last roll angle $\theta_{roll,SL}$:

$$\begin{aligned}
&\vec{a}_{SL}^{B} = {}^{B}T_{SL}^{L}\cdot\vec{a}_{SL}^{L} = \\
&\begin{bmatrix} 1 & 0 & 0 \\ 0 & \cos\theta_{roll,SL} & \sin\theta_{roll,SL} \\ 0 & -\sin\theta_{roll,SL} & \cos\theta_{roll,SL} \end{bmatrix} \cdot \begin{bmatrix} \cos\theta_{pitch,SL} & 0 & -\sin\theta_{pitch,SL} \\ 0 & 1 & 0 \\ \sin\theta_{pitch,SL} & 0 & \cos\theta_{pitch,SL} \end{bmatrix} \cdot \begin{bmatrix} \cos\theta_{yaw,SL} & \sin\theta_{yaw,SL} & 0 \\ -\sin\theta_{yaw,SL} & \cos\theta_{yaw,SL} & 0 \\ 0 & 0 & 1 \end{bmatrix} \cdot \vec{a}_{SL}^{L}
\end{aligned} \tag{7}$$

The rotation matrix $^{L}T_{SL}^{I}$ transforms a vector $\vec{a}_{SL}^{I}$ at orbit position SL_{OP} from **I** into **L**:

$$\vec{a}_{SL}^{L} = {}^{L}T_{SL}^{I}\cdot\vec{a}_{SL}^{I} = \begin{bmatrix} \hat{\vec{h}}_{SL}^{I} \times \hat{\vec{p}}_{SL}^{I} & -\hat{\vec{h}}_{SL}^{I} & -\hat{\vec{p}}_{SL}^{I} \end{bmatrix}^{T} \cdot \vec{a}_{SL}^{I}, \tag{8}$$

where $\vec{h}^{I} = \vec{r}^{I} \times \dot{\vec{r}}^{I}$ is the angular momentum vector that is normal to the orbital plane. The superscript $(\ )^T$ transposes a matrix or a vector, and ^ indicates a unit vector.

Under TZDS condition, the relative velocity vector $\vec{v}_{rel}^{L}$ is aligned with the x_B axis in **B**, and the monostatic yaw $\theta_{yaw,SL}$, and pitch $\theta_{pitch,SL}$ angles can be obtained from its x,y,z components [19]:

$$\begin{aligned}
\theta_{yaw,SL} &= \tan^{-1}\left(v_{rel,y}^{L} \big/ v_{rel,x}^{L}\right) \\
\theta_{pitch,SL} &= -\tan^{-1}\left(v_{rel,z}^{L} \Big/ \sqrt{\left(v_{rel,x}^{L}\right)^2 + \left(v_{rel,y}^{L}\right)^2}\right)
\end{aligned}. \tag{9}$$

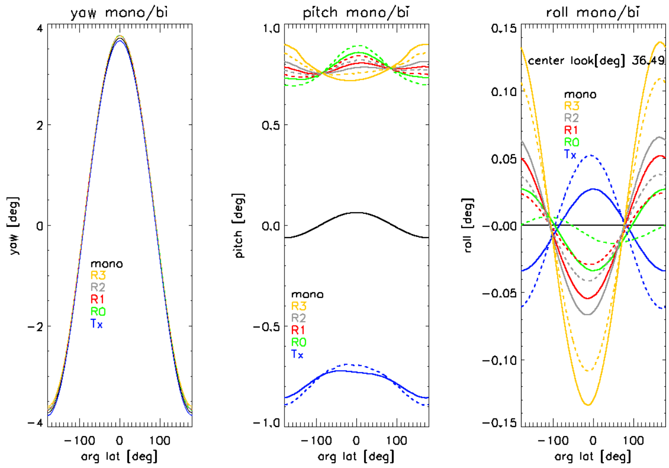

Figure 14 BZDS and S-CSL attitude steering angles. Monostatic TZDS angles in black color and BZDS angles of section III in continuous line style in blue (Tx) and green (Rx_0) color vs. argument of latitude. S-CSL steering angles for multistatic scenario of section IV, with CSL derived from Tx and Rx_0 satellite positions in continuous line style (Tx and Rx_0 steering angles are identical to BZDS), and with CSL derived from midpoint phase center PC_m in dashed line style.

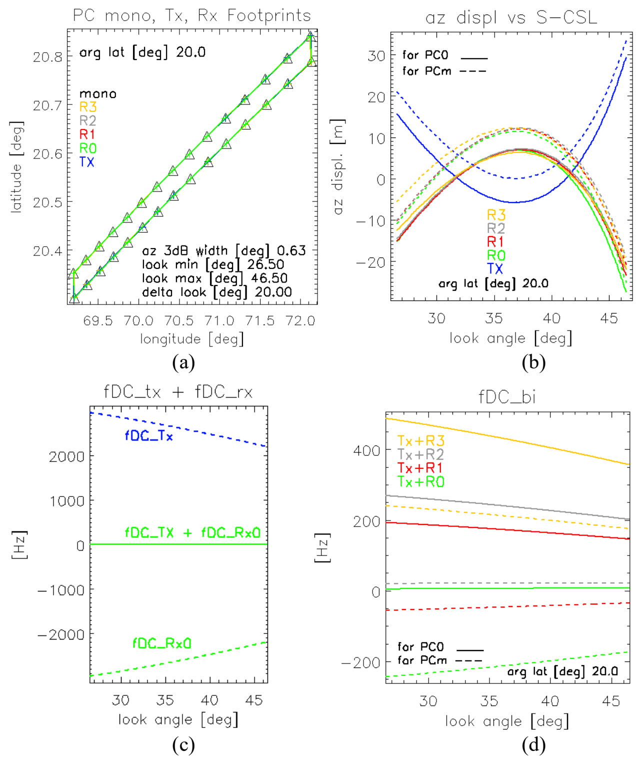

Figure 15 BZDS and S-CSL beam footprints and Doppler centroid, 20° look angle range. (a) Ground beam footprints for BZDS in black (Tx) and green (Rx_0) color. The other colors complement the footprints for multistatic S-CSL steering. The footprints from BZDS and multistatic S-CSL based on either the phase center PC_0 or the phase center PC_m are all on top of each other. (b) Beam footprint azimuth displacements w.r.t. S-CSL for PC_0 and PC_m. (c) Doppler centroids resulting from BZDS, $f_{DC,Tx}$ in transmit, $f_{DC,Rx}$ in receive by satellite Rx_0, and summation to bistatic $f_{DC,bi}$. (d) The $f_{DC,bi}$ of all bistatic pairs in multistatic S-CSL steering based on either PC_0 or PC_m.

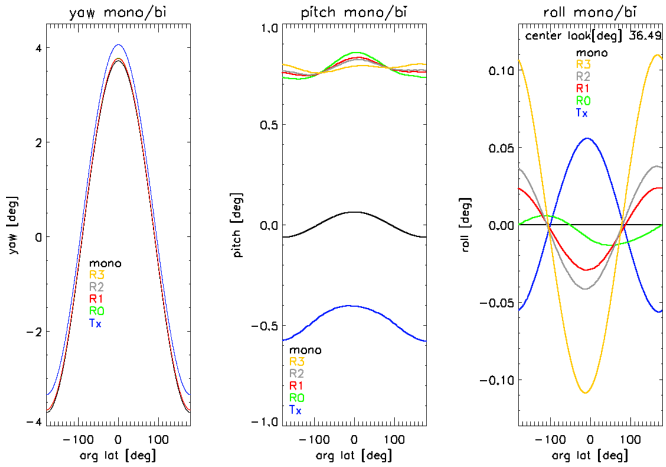

Figure 16 M-CSL attitude steering angles of section IV. The color coding for monostatic TZDS acquisition from PC_0 position (serves as reference value), and the satellites Tx, Rx_0, Rx_1, Rx_2, and Rx_3 for multi-static acquisition is equal in all plots of this section and also labeled in the plots.

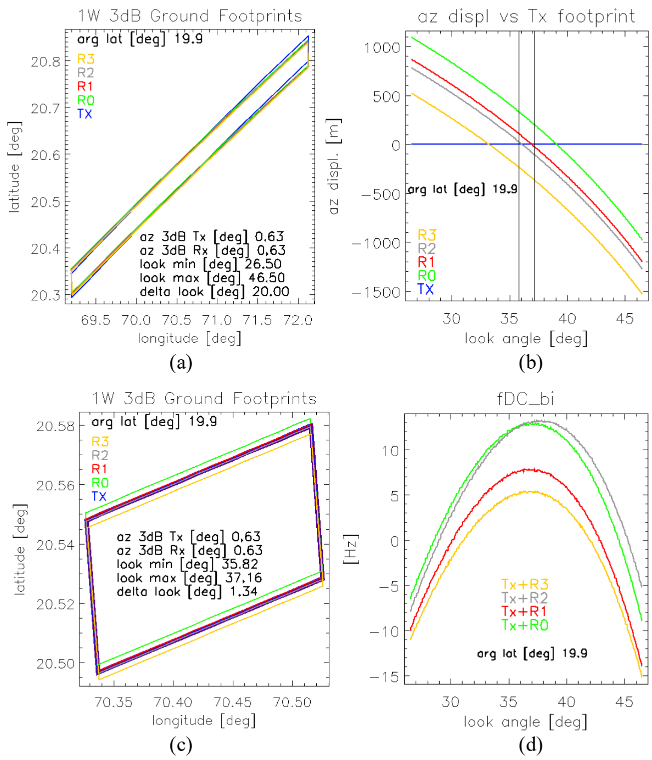

Figure 17 M-CSL beam footprints and Doppler centroid. (a) Ground beam footprints for M-CSL steering with 20° look angle range. (b) Azimuth position mismatch of Rx beams with respect to Tx swath for 20° look angle range. Vertical lines indicate the look angle range for 20 km swath width. (c) Beam footprints for 20 km swath width. In purple color and thick line style, the footprint from S-CSL steering of section IV.A.1 is added that is also derived from PC_m. (d) Bistatic Doppler centroids for M-CSL steering.

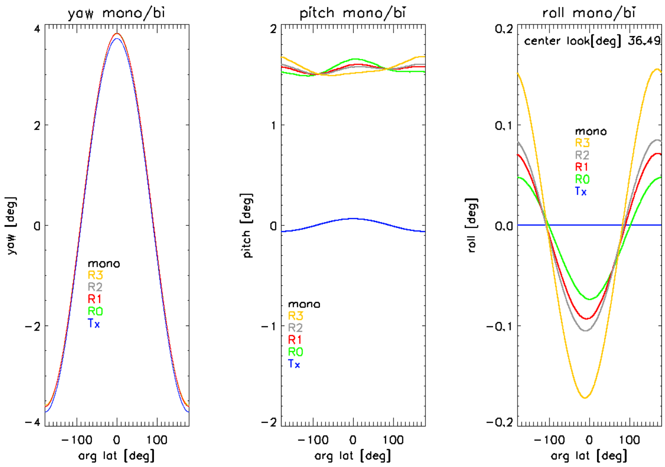

Figure 18 S-TSL attitude steering angles for multistatic scenario and supplementary acquisition.

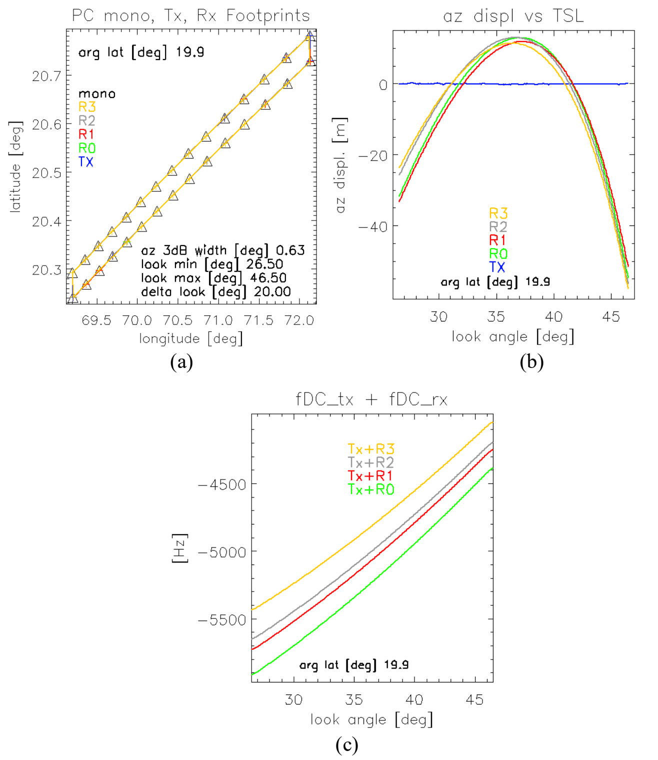

Figure 19 S-TSL beam footprints and Doppler centroid. (a) Footprints for S-TSL steering. (b) Azimuth displacement of Rx beams with respect to TSL. (c) Bistatic Doppler centroids for S-TSL steering.

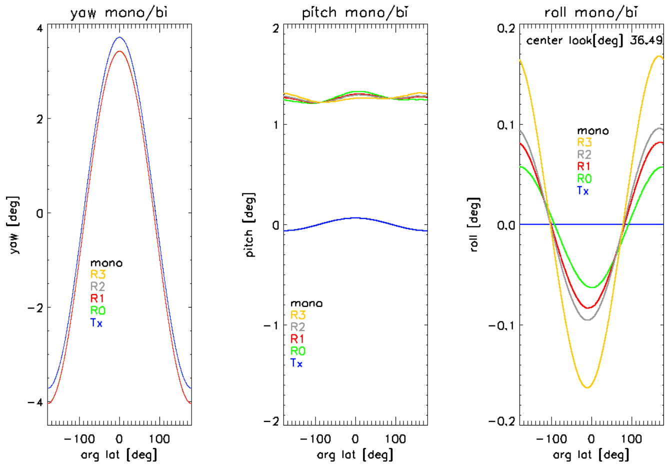

Figure 20 M-TSL attitude steering angles for multistatic scenario and supplementary acquisition.

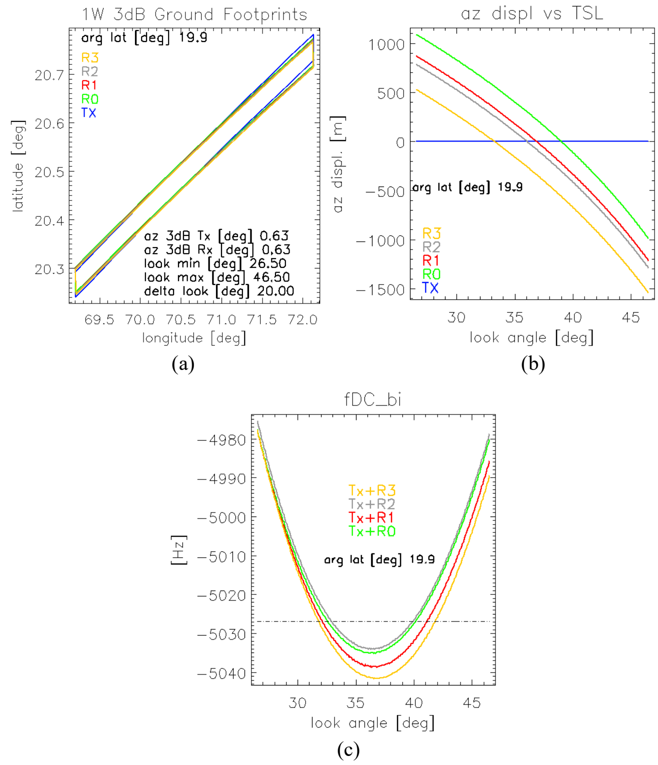

Figure 21 M-TSL beam footprints and Doppler centroid. (a) Ground beam footprints. (b) Azimuth position of Rx beams with respect to Tx swath. (c) Bistatic Doppler centroids. The Doppler centroid used in the steering angle optimization f_{DC,Bi_mean} is indicated by the dotted dashed line.

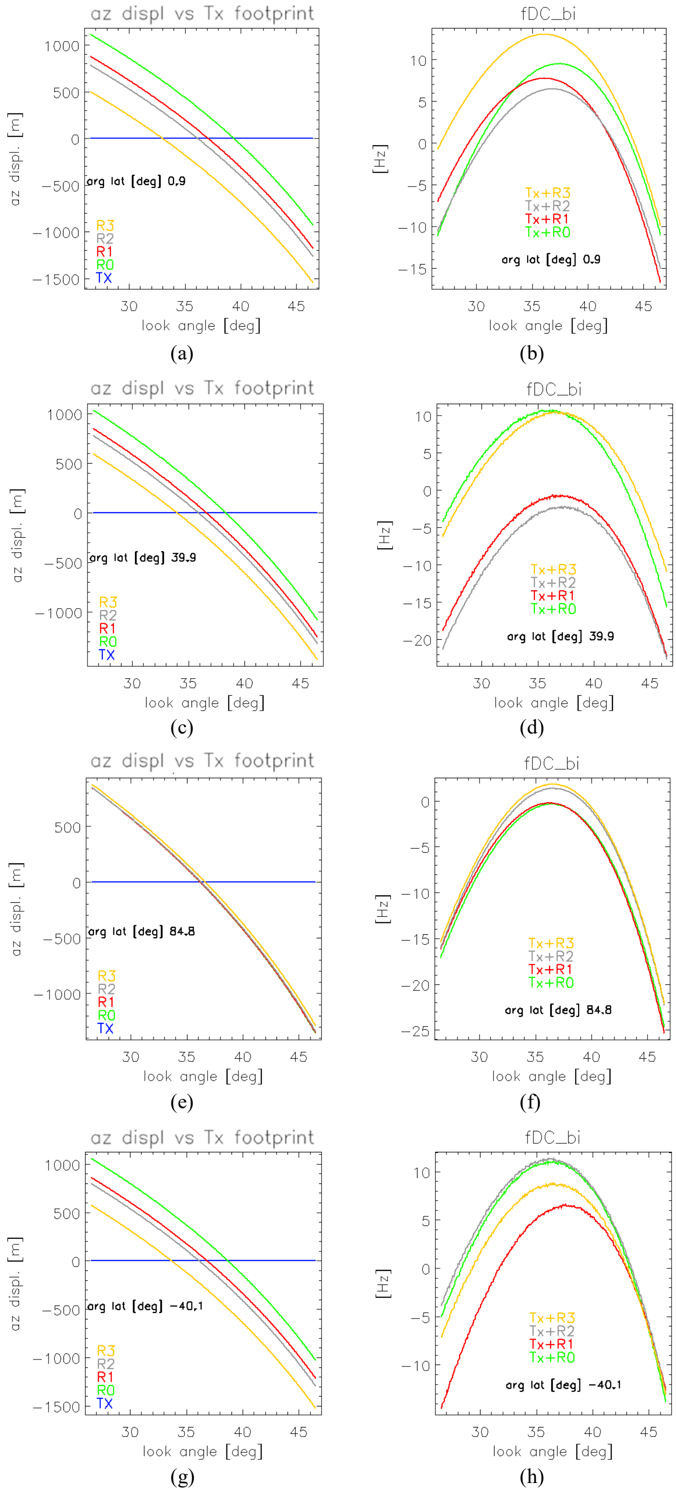

Figure 22 Beam azimuth displacement and bistatic Doppler centroids for M-CSL steering at different orbit positions. (a)(b) for ~0° argument of latitude, (c)(d) for ~40°, (e)(f) for ~85°, (g)(h) for ~-40°.

B. Approximated Analytical Derivation of Multistatic Yaw and Pitch Angles for Single Swath Line Steering.

Figure 23 shows the underlying geometry for the derivation with the SL orbit position SL_{OP} and the orbit position of a DisPlaced satellite (DP_{OP}). The displacement corresponds to a baseline (refer to Figure 2 and Figure 3).

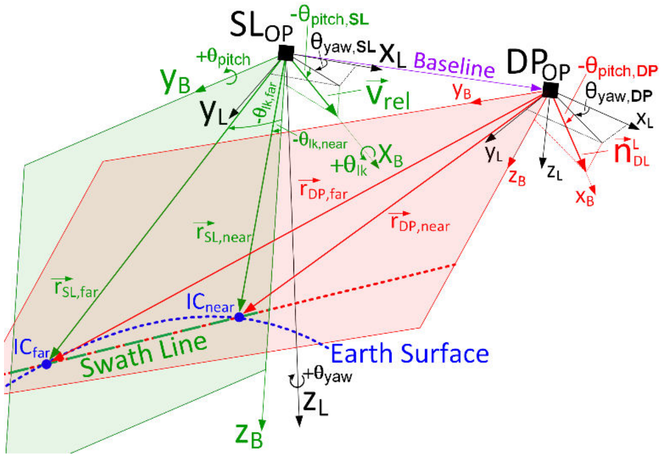

Figure 23 Analytical derivation of yaw $\theta_{yaw,DP}$ and pitch $\theta_{pitch,DP}$ angles at displaced orbit position (DP_{OP}) from the input yaw $\theta_{yaw,SL}$ and pitch $\theta_{pitch,SL}$ angles at the swath line defining orbit position (SL_{OP}) by means of near and far intersection points (IC).

The angles yaw $\theta_{yaw,SL}$, and pitch $\theta_{pitch,SL}$ at SL_{OP} are the input to the derivation of the yaw $\theta_{yaw,DP}$, and pitch $\theta_{pitch,DP}$ angles at DP_{OP}. As in the main part of our paper, $\theta_{yaw,SL}$ and $\theta_{pitch,SL}$ define a swath line on the Earth surface, and $\theta_{yaw,DP}$ and $\theta_{pitch,DP}$ are to be estimated to point from DP_{OP} to the same swath line. In the derivation, we apply the dependence between yaw and pitch angles and the normal vector of the plane formed by the near and far intersection points IC_{near} and IC_{far}, respectively, with the relevant satellite orbit position SL_{OP} or DP_{OP}. In (9), the normal vector is $\vec v^{L}_{rel}$ and the corresponding plane is shown in Figure 23 in green color. The normal vector of the red plane $\vec n^{L}_{DL}$ is to be calculated in **L** at DP_{OP}. This will provide the required angles $\theta_{yaw,DP}$ and $\theta_{pitch,DP}$ in analogy to (9).

We start the analytical derivation in **B** at SL_{OP} and define an initial pointing vector $\hat{\vec r}^{B}_{SL} = [0,0,1]^T$. We assume no additional antenna steering in azimuth or elevation. The elevation angle and the look angle are both considered to describe rotations around the x_B-axis. We summarize both angles into the look angle θ_{lk} and substitute the roll angle $\theta_{roll,SL}$ in (7) by θ_{lk}. Then, we can express the pointing vector in **L** at the SL_{OP} for the near/far look angles $\theta_{lk,near/far}$ by

$$\hat{\vec r}^{L}_{SL,near/far} = \left[{}^{B}T^{L}_{SL}\right]^{T} \cdot \hat{\vec r}^{B}_{SL} = {}^{L}T^{B}_{SL} \cdot [0 \quad 0 \quad 1]^{T}$$
$$= \begin{bmatrix} \cos\theta_{yaw,SL}\cdot\sin\theta_{pitch,SL}\cdot\cos\theta_{lk,near/far} - \sin\theta_{yaw,SL}\cdot\sin\theta_{lk,near/far} \\ \sin\theta_{yaw,SL}\cdot\sin\theta_{pitch,SL}\cdot\cos\theta_{lk,near/far} + \cos\theta_{yaw,SL}\cdot\sin\theta_{lk,near/far} \\ \cos\theta_{pitch,SL}\cdot\cos\theta_{lk,near/far} \end{bmatrix}, \tag{10}$$

Next, the unit vectors $\hat{\vec r}^{L}_{SL,near/far}$ are lengthened and intersected with the Earth surface. Both lengths $k_{near/far}$ of the resulting vectors $\vec r^{L}_{SL,near/far}$ from SL_{OP} to the intersections $IC_{near/far}$ can be calculated by

$$k_{near/far}\left(\theta_{pitch,SL},\theta_{lk,near/far};h_{loc};r_{E,loc}\right) = \left(r_{E,loc}+h_{loc}\right)\cdot\cos\theta_{pitch,SL}\cdot\cos\theta_{lk,near/far}$$
$$-\sqrt{\left(r_{E,loc}+h_{loc}\right)^{2}\cdot\left[\left(\cos\theta_{pitch,SL}\cdot\cos\theta_{lk,near/far}\right)^{2}-1\right]+r^{2}_{E,loc}} \tag{11}$$

The approximation of a spherical Earth is made with a local radius $r_{E,loc}$ and a resulting satellite altitude h_{loc} at SL_{OP}. Note, the length $k_{near/far}$ is independent of the yaw angle $\theta_{yaw,SL}$ due to the local spherical approximation.

In the next step, the vectors $\vec{r}^{L}_{DP,near/far}$ from DP_{OP} to $IC_{near/far}$ in **L** at DP_{OP} are calculated with

$$\vec{r}^{L}_{DL,near/far} = {}^{L}T^{I}_{DP} \cdot \left(\vec{p}^{I}_{SL} + {}^{I}T^{L}_{SL} \cdot k_{near/far} \cdot \hat{\vec{r}}^{L}_{SL,near/far} - \vec{p}^{I}_{DP} \right) \cdot \tag{12}$$

The vectors $\vec{r}^{L}_{DP,near/far}$ define the red intersection plane shown in Figure 23. We build the normal vector $\vec{n}^{L}_{DL}$ to that plane, and the yaw $\theta_{yaw,DP}$, and pitch $\theta_{pitch,DP}$ angles at the displaced orbit position DP_{OP} result from its components

$$\begin{aligned} \vec{n}^{L}_{DP} &= \left[n^{L}_{DP,x} \quad n^{L}_{DP,y} \quad n^{L}_{DP,z} \right]^{T} = \vec{r}^{L}_{DL,far} \times \vec{r}^{L}_{DL,near}. \\ \theta_{yaw,DP} &= \tan^{-1}\left(n^{L}_{DP,y} / n^{L}_{DP,x} \right) \\ \theta_{pitch,DP} &= \tan^{-1}\left(n^{L}_{DP,z} \middle/ \sqrt{\left(n^{L}_{DP,x}\right)^{2} + \left(n^{L}_{DP,y}\right)^{2}} \right) \end{aligned} \tag{13}$$

For the case of Single Central Swath Line (S-CSL) steering that is described in section IV.A.1), the approximated analytical solution for the yaw and pitch angles are compared to the numerical results of Figure 14. A specific case has been selected, where the orbit position SL_{OP} is in-between the Tx and Rx_0 satellite positions (continuous line style in Figure 14). The DL_{OP} orbit position is set to each of the Tx, Rx_0, Rx_1, Rx_2, or Rx_3 positions. The yaw and pitch angles derived by the numerical and approximated analytical approach are provided in Figure 24. The results fit well apart from a small deviation for larger cross-track baselines, which can be explained with the approximation in the analytical derivation.

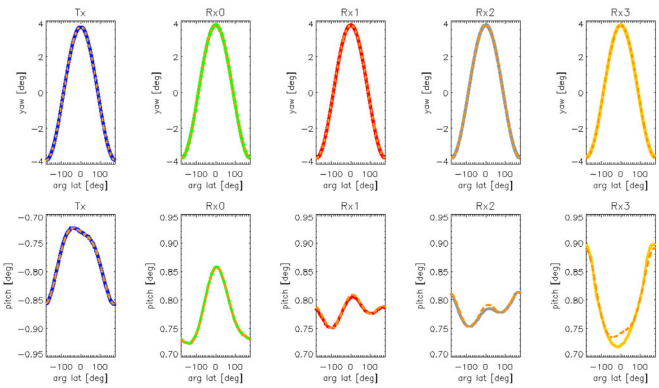

Figure 24 Multistatic yaw and pitch angles for S-CSL acquisition with swath line calculation from the orbit position between Tx and Rx_0 satellites. The numerical results are provided in the identical satellite coloring as used in Figure 14. The approximated analytical results obtained from (13) are plotted in dashed line style and orange color.

C. Analytical Dependence of Doppler Centroid and Squint Angle from Yaw, Pitch and Look Angles and Earth Rotation.

In (3) of [19] the (residual) Doppler centroid f_{DC} is calculated from the relative velocity vector $\vec{v}^{I}_{rel}$ and the unit direction vector from satellite to an arbitrary target $\hat{\vec{r}}^{I}$. We presume the Doppler centroid to arise at the center azimuth beam illumination of a target. Taking into account the above used rotational sequence and (5), (8) and (10), the analytical dependence of the Doppler centroid f_{DC} from yaw θ_{yaw}, pitch θ_{pitch}, and look θ_{lk} angles and the Earth rotational speed can be derived to be

$$\begin{aligned} f_{DC}\left(\theta_{yaw}, \theta_{pitch}, \theta_{lk}, \omega_{E}\right) &= -\frac{q}{\lambda} \cdot \vec{v}^{I}_{rel} \cdot \hat{\vec{r}}^{I} \\ &= -\frac{q}{\lambda} \cdot \left(\dot{\vec{p}}^{I} - \vec{\varpi}^{I}_{E} \times \vec{p}^{I} \right) \cdot {}^{I}T^{L} \cdot \begin{bmatrix} \cos\theta_{yaw} \cdot \sin\theta_{pitch} \cdot \cos\theta_{lk} - \sin\theta_{yaw} \cdot \sin\theta_{lk} \\ \sin\theta_{yaw} \cdot \sin\theta_{pitch} \cdot \cos\theta_{lk} + \cos\theta_{yaw} \cdot \sin\theta_{lk} \\ \cos\theta_{pitch} \cdot \cos\theta_{lk} \end{bmatrix} \end{aligned} \tag{14}$$

with $q = 2$ for monostatic

$q = 1$ for both bistatic Doppler components $f_{DC,Tx}$ and $f_{DC,Rx}$

In (14), a set of θ_{yaw}, θ_{pitch}, and θ_{lk} angles causes a pointing direction, and the Doppler centroid into that direction can be calculated. The pointing direction can also be calculated from a target position and the satellite position at the target azimuth center beam illumination. Note that, apart from assuming the roll and look angles to describe rotations around the same axis, there is no further approximation in (14).

From the scalar product in (14) a squint angle ψ can be defined in the first line of (15) being $\pi/2$ minus the angle between $\vec{v}^{I}_{rel}$ and $\hat{\vec{r}}^{I}$ in the inertial system **I**:

$$\begin{aligned} f_{DC}\left(\theta_{yaw}, \theta_{pitch}, \theta_{lk}, \omega_{E}\right) &= -\frac{q}{\lambda} \cdot \vec{v}^{I}_{rel} \cdot \hat{\vec{r}}^{I} = -\frac{q}{\lambda} \cdot v^{I}_{rel} \cdot \sin(\psi) \quad = f_{DC}\left(v^{I}_{rel}, \psi\right) \\ &= f_{DC}\left(v^{EF}_{S}, \psi\right) = -\frac{q}{\lambda} \cdot v^{EF}_{S} \cdot \sin(\psi) = -\frac{q}{\lambda} \cdot \vec{v}^{EF}_{S} \cdot \hat{\vec{r}}^{EF} \end{aligned} \tag{15}$$

At the beginning of this appendix, we showed that the magnitudes of the velocities v^{I}_{rel} and v^{EF}_{S} are equal. Therefore, ψ can also be obtained in the Earth fixed system **EF** from the direction vector $\hat{\vec{r}}^{EF}$ from satellite to target, and the satellite velocity vector $\vec{v}^{EF}_{S}$.

Eqs. (14) and (15) are applied to a monostatic acquisition from orbit position SL_{OP} at 20° argument of latitude in the S-CSL steering example. Figure 25 provides in the plots (a) and (c) the resulting Doppler centroid and squint angle for $\theta_{yaw} = \theta_{pitch} = 0°$ as a function of look angle. This is the result without any Doppler steering. Applying the TZDS angles results in the plots (b) and (d) with a zero Doppler centroid and zero squint angle along the whole look angle range, as expected.

If we use (14) to calculate the Doppler centroid for the case of the multistatic S-CSL acquisition, and we insert the numerically calculated yaw and pitch angles for the Tx and Rx_0 satellites, we obtain the Doppler centroid components in Figure 26 (a). This result is identical to the one of Figure 15 (c). The bistatic Doppler centroid is the sum of $f_{DC,Tx}$ and $f_{DC,Rx0}$ components and is almost zero Hz along the whole look angle range. Figure 26 (b) completes the results for the other receiving satellites, which correspond to the ones of Figure 15 (d) in continuous line style.

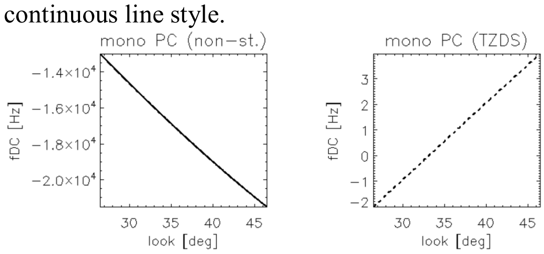

(a) (b)

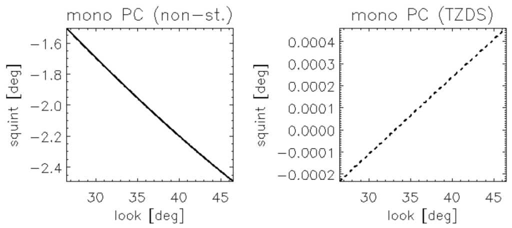

(c) (d)

Figure 25 Calculation of monostatic Doppler centroid and squint angle with (14) and (15) for the S-CSL example at SL_{OP} orbit position at 20° argument of latitude. (a) and (c) without Doppler steering. (b) and (d) with the TZDS yaw and pitch angles.

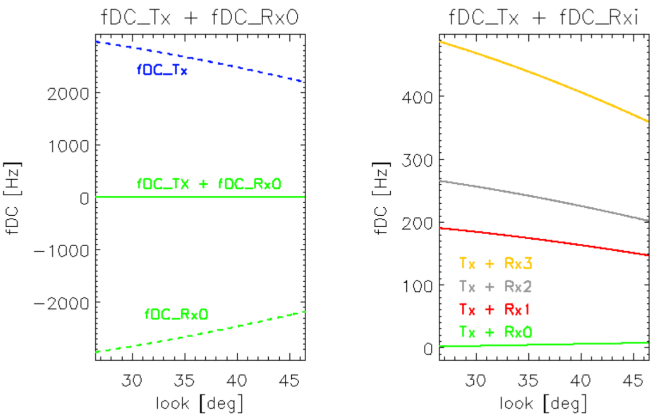

(a) (b)

Figure 26 Multistatic Doppler centroid for S-CSL acquisition for 20° argument of latitude as calculated from (14) after insertion of the numerically calculated yaw and pitch angles $\theta_{yaw,DP}$, and pitch $\theta_{pitch,DP}$, respectively, with the DP_{OP} orbit position being set to the Tx, Rx_0, Rx_1, Rx_2 and Rx_3 orbit positions. (a) provides the individual Tx and Rx_0 Doppler centroid components. (b) provides the bistatic Doppler centroids for all multistatic combinations.

Eq. (14) can be used to support the numerical calculation of the attitude steering angles in the multiple swath line cases by calculation of intermediate Doppler centroid values for Tx and Rx_i satellite positions (cf. Figure 12 and Figure 13). However, this means that the Earth surface shape (the Ellipsoid and its elevation - Digital Elevation Model) is not included in the calculation of the attitude angles, which causes some inaccuracies. As can be derived from Figure 26, only the monostatic acquisition from SL_{OP} is independent of the look angle and the elevation of the Earth surface. This is not the case for the bistatic acquisition, where the Tx and Rx_i components depend on the ground target's elevation. The dependency is introduced by the tilt of the plane of the constant Doppler centroid component (red plane in Figure 26) with respect to the plane that defines the swath line (green plane in Figure 26). However, (14) can be used to calculate the initial values of the multistatic attitude angles in the numerical calculation, or to provide approximative multistatic attitude angles.

ACKNOWLEDGMENT

The authors would like to thank Ralph Kahle from DLR/GSOC and Allan Bojarski from DLR/HR for discussions on helix orbits. Furthermore, Ralph Kahle supported in the calculation of the argument of latitude.

The authors would like to thank the reviewers who contributed to the improvement of the manuscript.

REFERENCES

[1] H. Fiedler, E. Boerner, J. Mittermayer, and G. Krieger, “Total zero Doppler steering—A new method for minimizing the Doppler centroid,” IEEE Geosci. Remote Sens. Lett., vol. 2, no. 2, pp. 141–145, Apr. 2005.

[2] Gerhard Krieger, Mariantonietta Zonno, Josef Mittermayer, Alberto Moreira, Sigurd Huber, Marc Rodriguez-Cassola, “MirrorSAR: A Fractionated Space Transponder Concept for the Implementation of Low-Cost Multistatic SAR Missions”, Proc. of EUSAR 2018, Aachen, 2018.

[3] Josef Mittermayer, Paco López-Dekker, Thomas Kraus, Gerhard Krieger, “Small Satellite Dispersed SAR - an Exemplary Configuration”, Proc. of EUSAR 2016, Hamburg, Germany.

[4] S. Wollstadt and J. Mittermayer, “Nadir Margins in TerraSAR-X Timing Commanding”, Proc. of CEOS SAR Calibration and Validation Workshop, 2008.

[5] J. C. Curlander and R. McDonough, Synthetic Aperture Radar. New York: Wiley, 1991.

[6] A. Zurita and J. Closa, “Iso-Doppler Steering Technique in Multistatic SAR”, Proc. of EUSAR 2018, Aachen, Germany.

[7] R. Kahle, B. Kazeminejad, M. Kirschner, Y. Yoon, R. Kiehling, and S. D’Amico, “First in-orbit experience of TerraSAR-X flight dynamics operations,” in *Proc. 20th Int. Symp. Space Flight Dyn.*, Annapolis, MD, Sep. 24–28, 2007.

[8] J. Mittermayer, B. Schättler, and M. Younis, “TerraSAR-X commissioning phase execution summary”, IEEE Trans. Geosci. Remote Sens., vol. 48, no. 2, pp. 649–659, Feb. 2010.

[9] J. Mittermayer, M. Younis, R. Metzig, S. Wollstadt, J. Márquez Martínez, and A. Meta, “TerraSAR-X system performance characterization and verification,” IEEE Trans. Geosci. Remote Sens., vol. 48, no. 2, pp. 660–676, Feb. 2010.

[10] G. Krieger, A. Moreira, H. Fiedler, I. Hajnsek, M. Werner, M. Younis, M. Zink: ”TanDEM-X: A Satellite Formation for High Resolution SAR Interferometry”, IEEE Transactions on Geoscience and Remote Sensing, vol. 45, no. 11, pp. 3317 – 3341, 2007.

[11] P. López-Dekker, F. De Zan, T. Börner, G. Krieger, and A. Moreira, “Passive formation flying ATI-SAR for ocean currents observations: The PICOSAR concept,” in Proc. 1st Int. Earth Observ. Convoy Constellation Concepts Workshop (ESA-ESTEC), Noordwijk, The Netherlands, Oct. 2013, pp. 1–7.

[12] T. Börner, P. López Dekker, G. Krieger, M. Bachmann, A. Moreira, H. Müller “Passive Interferometric Ocean Currents Observation Synthetic Aperture Radar (PICOSAR)”, 9th IAA Symposium on Small Satellites for Earth Observation, 2013.

[13] P. Lopez-Dekker, H. Rott, S. Solberg, M. Zonno, M. Rodriguez-Cassola, P. Prats-Iraola, A. Moreira, “Companion SAR constellations for single-pass interferometric applications: The SESAME mission”, Proc. of IGARSS 2017.

[14] N. Gebert, B. Crnicero Dominguez, M. Davidson, M. Diaz martin, P. Sivestrin, “SAOCOM-CS – A passive companion to SAOCOM for single-pass L-band SAR interferometry”, Proc. of EUSAR 2014.

[15] M. Villano, A. Moreira, H. Miller, H. Rott, I. Hajnsek, R. Bamler, P. Lopez-Dekker, T. Börner, F. De Zan, G. Krieger, K. Papathanassiou, “SIGNAL: Mission Concept and Performance Assessment”, Proc. EUSAR 2010.

[16] A. Moreira, G. Krieger, and J. Mittermayer, “Satellite configuration for interferometric and/or tomographic remote sensing by means of synthetic aperture radar (SAR),” U.S. Patent 6 677 884, U.S. Off. Pat. Office, Washington, DC, Jul. 2002.

[17] D. Massonnet, “Capabilities and Limitations of the Interferometric Cartwheel”, TGRS, Vol. 39, No. 3, March 2001.

[18] D. Geudtner, M. Zink, Ch. Gierull, and S. Shaffer, “Interferometric alignment of the X-SAR antenna system on the Space Shuttle Radar Topography Mission”, IEEE Trans. Geoscience and Remote Sensing, Vol. 40, No. 5, pp. 995-1006, May 2002.

[19] Daniel P. Scharf, “Analytic Yaw-Pitch Steering for Side-Looking SAR with Numerical Roll Algorithm for Incidence Angle”, IEEE Trans. Geoscience and Remote Sensing, Vol. 50, No. 9, pp. 3587-3594, Sept 2012.

[20] Z. Yu, Y. Zhou, J. Chen, and C. Li, “A new satellite attitude steering approach for zero Doppler centroid,” in *Proc. IET Conf. Publ.*, 2009, no. CP551, p. 593.

Josef Mittermayer received the Dipl.-Ing. (M.Sc.) degree in electrical engineering from the Technical University of Munich, Munich, Germany, in 1995, the M.Sc. degree in space system engineering from the Delft University of Technology, Delft, The Netherlands, in 2004, and the Ph.D. degree from the University of Siegen, Siegen, Germany, in 2000.

Since 1994 he is with the Microwaves and Radar Institute, German Aerospace Center (DLR), Oberpfaffenhofen, Germany. From 2002 to 2008 he worked in the TerraSAR-X project, from 2004 to 2008 also in the TerraSAR-X group leader position. Additionally, he was the project manager of *TerraSAR-X System Engineering and Calibration*, and was technically responsible for the TerraSAR-X commissioning phase. His scientific and engineering work includes the fields SAR processing, SAR system engineering, and SAR mode development. Currently, NewSpace and formations of small multistatic SAR satellites is a focus of his work. Apart from numerous conference papers and patents in the field of SAR, Dr. Mittermayer is author or co-author of more than 20 peer-reviewed journal papers.

Dr. Mittermayer and his colleagues were recipients of the IEEE Geoscience and Remote Sensing Society Transactions Prize Paper Award for a paper on air and spaceborne stripmap and ScanSAR processing in 1996. He was a recipient of the DLR Science Award in 2001 for his work on spotlight-SAR processing. In 2011, he was awarded with the DLR *Forschungssemester* for his contribution to the TerraSAR-X project.

Gerhard Krieger (M'04-SM'09-F'13) received the Dipl.-Ing. (M.S.) and Dr.-Ing. (Ph.D.) (Hons.) degrees in electrical and communication engineering from the Technical University of Munich, Germany, in 1992 and 1999, respectively.

From 1992 to 1999, he was with the Ludwig Maximilians University, Munich, where he conducted multidisciplinary research on neuronal modeling and nonlinear information processing in biological and technical vision systems. Since 1999, he has been with the Microwaves and Radar Institute of the German Aerospace Center (DLR), Oberpfaffenhofen, Germany, where he started as a research associate developing signal processing algorithms for a novel forward-looking radar system employing digital beamforming on receive. From 2001 to 2007, he led the New SAR Missions Group which pioneered the

development of advanced bistatic and multistatic radar systems, such as TanDEM-X, as well as innovative multichannel SAR techniques and algorithms for high-resolution wide-swath SAR imaging. Since 2008, he has been the Head of the Radar Concepts Department which hosts about 40 scientists focusing on new SAR techniques, missions and applications. He has moreover been serving as Mission Engineer for TanDEM-X and he made also major contributions to the development of the Tandem-L mission concept, where he led the Phase-0 and Phase-A studies. Since 2019, he is also a professor at the Friedrich-Alexander-University Erlangen, Germany. Gerhard Krieger is author or co-author of more than 90 peer-reviewed journal papers, 9 invited book chapters, about 400 conference papers, and more than 15 patents.

Prof. Krieger has been an Associate Editor for the IEEE Transactions on Geoscience and Remote Sensing since 2012. In 2014, he served as the Technical Program Chair for the European Conference on Synthetic Aperture Radar and as a Guest Editor for the IEEE Journal of Selected Topics in Applied Earth Observations and Remote Sensing. He received several national and international awards, including the W.R.G. Baker Prize Paper Award from the IEEE Board of Directors, two Transactions Prize Paper Awards of the IEEE Geoscience and Remote Sensing Society, and two Best Paper Awards at the European Conference on Synthetic Aperture Radar.

Steffen Wollstadt received the Dipl.-Ing. (M.Sc.) degree in electrical engineering from the Technical University of Darmstadt, Darmstadt, Germany in 2005, with a thesis on metamaterial-based microstrip antenna design. In 2006 he joined the Microwaves and Radar Institute of the German Aerospace Center (DLR), Oberpfaffenhofen, Germany.

From 2006 to 2008, he was with the Satellite SAR Systems department as project engineer in the System Engineering and Calibration part of the TerraSAR-X ground segment, where he worked on the TerraSAR-X and TanDEM-X instrument command generation. He was the responsible for the commanding of experimental TOPS imaging mode acquisitions with TerraSAR-X.

From 2009 to 2017, he was with the Radar Concepts department of the Microwaves and Radar Institute in the SAR Missions research group, where he was mainly working on studies and projects about SAR instrument design, performance investigations and consulting, as well as design and improvement of novel SAR imaging modes. Furthermore, he worked on various experiments with TerraSAR-X and TanDEM-X about novel imaging modes and SAR performance improvement.

In 2018, he changed the position in the institute and took over the position of the head of administration and central services. Since then he mainly supports the institute and the projects on administrative level. His research interests are still on spaceborne SAR mission and instrument analysis as well as on interferometric problems, including along-track, repeat-pass and differential interferometry.